



# Inter-species variabilities of droplet transport, size change, and deposition in human and rat respiratory systems: An *in silico* study

Hamideh Hayati<sup>a</sup>, Yu Feng<sup>a,\*</sup>, Myron Hinsdale<sup>b</sup>

<sup>a</sup> School of Chemical Engineering, Oklahoma State University, Stillwater, OK, USA

<sup>b</sup> Department of Physiological Sciences, Oklahoma State University, Stillwater, OK, USA

## ARTICLE INFO

### Keywords:

Inter-species variability  
Droplet deposition  
Rat and human respiratory systems  
Euler-Lagrange  
Condensation and evaporation  
Precise rat-to-human scale-up method

## ABSTRACT

To speculate on human responses from animal studies, scale-up factors (body weight, lung volume, or lung surface area ratios) are currently used to extrapolate aerosol lung deposition from animal to human. However, those existing scale-up methods between animals and humans neglected two important inter-subject variability factors: (1) the effect of anatomical differences in respiratory systems from mouth/nose to peripheral lungs between human and rat, and (2) the effect of spatial distributions and temporal evolutions of temperature and relative humidity (RH) on droplet size change dynamics between the two species. To test the above-mentioned inter-species variability effects on droplet fates in pulmonary routes and generate correlations as a precise scale-up method for lung deposition estimation, this study simulated the transport of pure-water droplets in both human and Sprague-Dawley (SD) rat respiratory systems. Employing an experimentally validated Euler-Lagrange based Computational Fluid-Particle Dynamics (CFPD) model, simulations were performed for droplets with  $Stk/Fr$  between  $8.36 \times 10^{-5}$  and  $1.25 \times 10^{-2}$ . Droplets were inhaled through human and rat nostrils under resting breathing conditions. Numerical results indicate that RH becomes uniformly distributed in rat airways sooner than in human airways, which significantly influences droplet size change dynamics and the resultant droplet trajectories in pulmonary routes. Using the Stokes-Froude dimensionless number group (i. e.,  $Stk/Fr$ ) as the independent variable, the regional deposition fractions (DFs) and evaporation fractions (EFs) in both rat and human respiratory systems collapsed into unified correlations. Such correlations can be used for the new rat-to-human scale-up method, estimating the lung depositions with consideration of anatomical differences. Furthermore, the necessity to employ realistic RH and temperature boundary conditions (BCs) at airway walls was also confirmed for the accurate prediction of droplet size change using CFPD model. Employing idealized BCs leads the droplets to evaporate slower and deposit more than using realistic RH and temperature BCs.

## 1. Introduction

Animals such as rats and mice are frequently studied as human surrogates to investigate the toxic or therapeutic effects of inhaled aerosols. This is because the blood osmolality and body temperature (Clarkson, Magee, & Brenner, 2011) in rat airways are similar to those in human airways. Animal study data are subsequently scaled up to project human responses to the inhaled aerosols. However, the existing scale-up methods using human-to-rat bodyweight or lung surface area ratios are not accurate (Hayati & Feng, 2020;

\* Corresponding author.

E-mail address: [yu.feng@okstate.edu](mailto:yu.feng@okstate.edu) (Y. Feng).

<https://doi.org/10.1016/j.jaerosci.2021.105761>

Received 9 November 2020; Received in revised form 14 January 2021; Accepted 14 January 2021

Available online 23 January 2021

0021-8502/© 2021 Elsevier Ltd. All rights reserved.

## Nomenclature

### Acronym

BC	Boundary condition
CFPD	Computational fluid particle dynamics
DF	Deposition fraction
EF	Evaporation fraction
G	Generation
GR	Growth ratio
IAV	Influenza A virus
MSD	Mean squared deviation
RH	Relative humidity

### Symbols

$A_p$	Droplet surface area
$C_{Dp}$	Drag coefficient
$C_m$	Fuchs-Knudsen number coefficient
$c_p$	Specific heat of gas mixture
$c_{p,p}$	Specific heat of droplet
$D_{in}$	Inlet hydraulic diameter
$D_w$	Molecular diffusivity of water
$D_{w,t}$	Turbulent molecular diffusivity of water
$d_p$	Droplet diameter
$d_{p,f}$	Final diameter of droplet
$d_{p,i}$	Initial diameter of droplet
Fr	Froude number
$F_i^D$	Drag force
$F_i^L$	Lift force
$F_i^{BM}$	Brownian motion induced force
$F_i^G$	Gravity
$\vec{g}$	Gravitational acceleration
$H_{lat}$	Latent heat
H	Convective heat transfer coefficient of water
Kn	Knudsen number
$k_{hc}$	Modified thermal conductivity
$k_c$	Thermal conductivity
$k_{c,t}$	Turbulent thermal conductivity
$k_{mc}$	Mass transfer coefficient
$M_w$	Water molecular weight
$m_p$	Droplet mass
Nu	Nusselt number
$n_s$	Mass flux of vaporizable component s
$\bar{n}_s$	Average mass flux of vaporizable component s
Pr	Prandtl number
$Pr_t$	Turbulent Prandtl number
$p_{eq}$	Equilibrium vapor pressure on droplet surface
$p_{sat}$	Saturation vapor pressure at droplet temperature
R	Gas constant
Re	Reynolds number
$Re_p$	Droplet Reynolds number
Sc	Schmidt number
$Sc_t$	Turbulent Schmidt number
Sh	Sherwood number
Stk	Stokes number
T	Temperature
$T_p$	Droplet temperature
t	Time
$u_i$	Flow velocity
$u_i^p$	Droplet velocity
$V^*$	Normalized velocity magnitude

$\bar{V}_w$	Partial molar volume of water in the solute
$v$	Inlet mean-flow velocity
$x_j$	Space in j direction
$y_w$	Mass fraction of water in gas-mixture
$y_{w,surf}$	Mass fraction of water on droplet surface
$y_{w,\infty}$	Mass fraction of water far from droplet

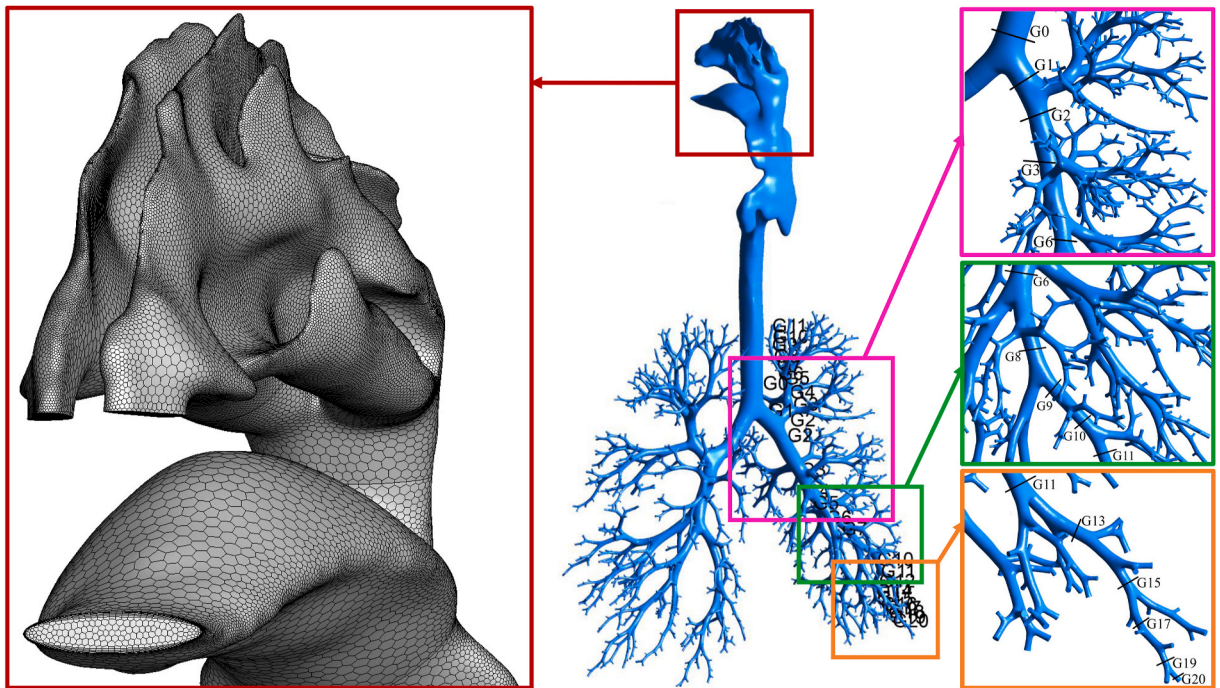
#### Greek Symbols

$\alpha_m$	Mass accommodation coefficient
$\gamma_w$	Activity coefficient of water
$\lambda$	Gas mixture mean free path
$\mu$	Viscosity at the gas mixture temperature
$\mu_t$	Turbulent viscosity at the gas mixture temperature
$\mu_{p,surf}$	Viscosity at the droplet surface temperature
$\rho$	Density of gas mixture
$\rho_w$	Density of water
$\sigma$	Surface tension
$\Phi_{vp}$	Viscous dissipation

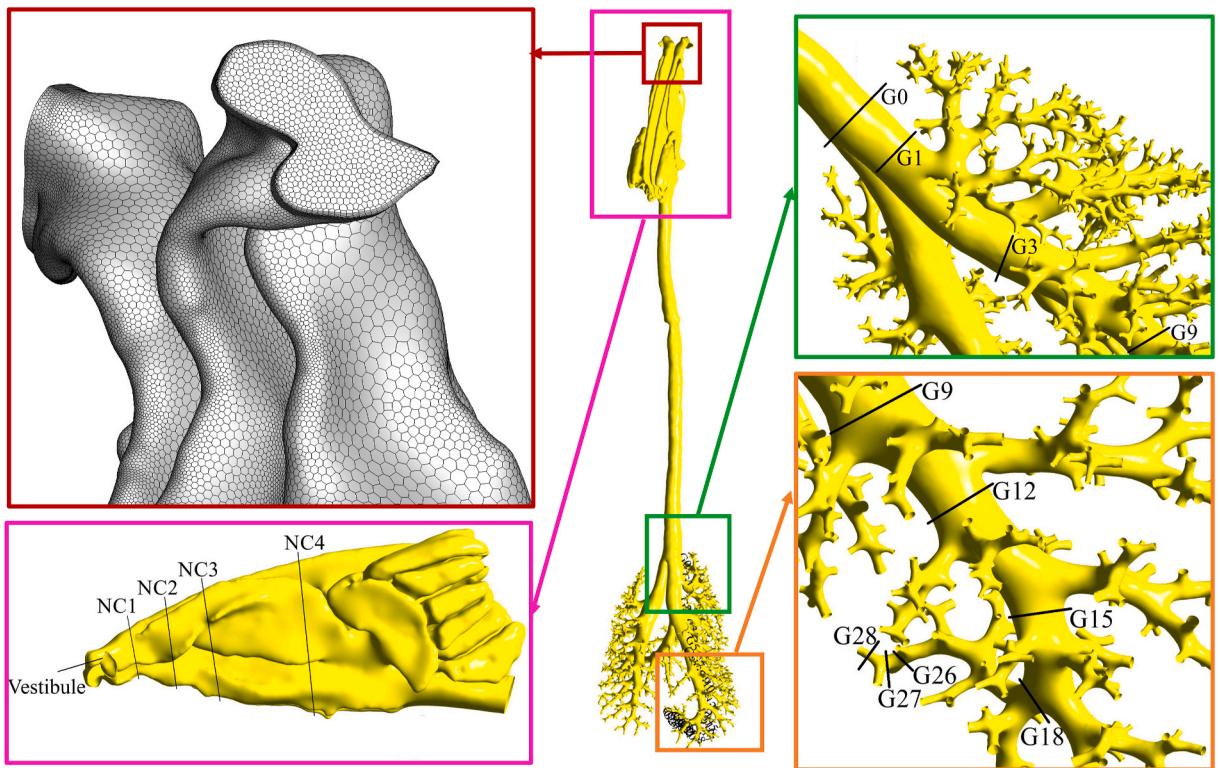
Nielsen & Koponen, 2018), since they neglect the effect of inter-species variabilities in airway anatomy, temperature, and humidity conditions. For example, the connecting angles between the nasal pharynx and trachea are different between human and rat (see Fig. 1), which will lead to different droplet transport and deposition in airways (Haghnegahdar, Feng, Chen, & Lin, 2018). Also, differences in localized relative humidity (RH) and temperature distribution in between human and rat airways will lead to different growth/shrinkage in droplet size in airways (Asgharian, 2004; Broday & Georgopoulos, 2001). Specifically, the partial pressure gradient of water vapor between the surroundings and the droplet surface, which drives evaporation and condensation mechanisms, must be considered in the scale-up method. The partial pressure gradient is also significantly influenced by temperature gradient and droplet diameter. The continuous changes in droplet size lead to variations in their diffusion, sedimentation and impaction, and time-dependent transport process during a breathing cycle (Asgharian, 2004; Ferron, Oberdorster, & Henneberg, 1989). Therefore, an accurate scale-up method between rat and human must consider the inter-species variabilities in airway anatomy, temperature, and humidity. To address the above-mentioned inter-species variabilities, accurate predictions of droplet transport, size change, and deposition in rat and human respiratory systems are needed.

Although there are existing *in vivo* and *in vitro* measurements on droplet depositions in airways or airway replica (Cheng et al., 1996; Dai, Chang, Tu, & Hsu, 2007; Gerde, Cheng, & Medinsky, 1991; Golshahi, Noga, Thompson, & Finlay, 2011; Kelly, Asgharian, Kimbell, & Wong, 2004; Kelly, Bobbitt, & Asgharian, 2001; Longest, Tian, & Hindle, 2011; Nikander, Prince, Coughlin, Warren, & Taylor, 2010; Stahlhofen, Rudolf, & James, 1989), it is very challenging to experimentally measure localized particle growth, dispersion, and deposition, due to the imaging resolution and ethical restrictions. Gerde et al. (1991) studied the deposition of ultrafine aerosols in the nasal airways of Fischer-344/N rats. Their results proved that nasal airway casts could be used to estimate the *in vivo* deposition of ultrafine aerosols. Kelly et al. (2001) conducted *in vivo* study to determine particle deposition efficiencies for the nasal airways in Long-Evans rats. Their results demonstrated the importance of considering fluid accelerations inherent in normal breathing when determining aerosol deposition dominated by inertial impaction.

Furthermore, while most *in vitro* studies on lung deposition focus on upper airway results due to the lack of imaging resolution and operation flexibilities, *in silico* studies were able to simulate the transport and deposition of inhaled particulate matter (PM) in different lung regions, including lower airways (Asgharian, 2004; Broday & Georgopoulos, 2001; Corley et al., 2012; Haghnegahdar, Zhao, & Feng, 2019; Kolanjiyil & Kleinstreuer, 2017; Longest et al., 2011; Luo & Liu, 2009; Tian, Longest, Li, & Hindle, 2013). Specifically, to provide accurate droplet depositions in rat and human airways for developing precise scale-up methods, computational fluid-particle dynamics (CFPD) models, as well as other numerical models, were applied to overcome the limitations of *in vivo* and *in vitro* studies. CFPD models can predict the laminar/turbulent particle-laden airflow, with the capability to track droplet size-change dynamics, transport, and deposition simultaneously in respiratory systems, and provide more accurate predictions of their trajectories and fates. However, most existing *in silico* efforts employed idealized temperature and RH boundary conditions (BCs) to predict the size change dynamics of inhaled droplets with different compositions. For example, Asgharian (2004) developed a mathematical model for the deposition of NaCl particles in asymmetric human tracheobronchial trees, in which they assumed  $T = 37\text{ }^\circ\text{C}$  and  $\text{RH} = 99.5\%$  constantly in the whole computational domain. Using the same idealized temperature and RH conditions ( $T = 37\text{ }^\circ\text{C}$ ,  $\text{RH} = 99.5\%$ ), Broday and Georgopoulos (2001) studied the growth and deposition of particles in human lungs. They reported the growth and evolution of the size distribution of particles with different compositions under typical lung conditions ( $T = 37\text{ }^\circ\text{C}$ ,  $\text{RH} = 99.5\%$ ). There are also other research papers that employed the idealized RH and temperature BCs in the airway to study the dynamics of inhaled drug particles and virus-laden droplets (Haghnegahdar et al., 2019). Longest et al. (2011); Tian et al. (2013) simulated the size change and deposition of submicron drug particles composed of insulin (poorly water-soluble) and sodium chloride (hygroscopic excipient) under different inhalation conditions using CFPD. They found that such a combination of submicron aerosols improves the delivery of the drugs to designated lung regions. Using idealized RH and temperature BCs with constant values may introduce errors in droplet size change predictions, since it has been claimed that the temperature and RH values are different at the airway boundaries in different



(a) Human Respiratory System



(b) Rat Respiratory System

**Fig. 1.** Geometry and mesh details of the human and rat respiratory systems: (a) Human respiratory system from mouth/nose to G20, (b) Rat respiratory system from nose to G28.

regions of the airways (Ferron, Upadhyay, Zimmermann, & Karg, 2013). Thus, to provide accurate droplet transport and deposition data for precise scale-up method development, it is necessary to employ physiologically realistic RH and temperature BCs and compare the CFPD simulation results with the predictions using idealized RH and temperature BCs.

In this paper, the objectives are (1) to develop an precise rat-to-human scale-up method for droplet delivered dose in respiratory systems, and (2) to test the central hypothesis, i.e., the delivered dose in the human respiratory system can be estimated based on the deposition data in the rat respiratory system by employing the correlations which can unify the deposition data in both human and rat as a function of droplets Stokes number (Stk) and Froude number (Fr) (Hayati & Feng, 2020; Kolanjiyil, Kleinstreuer, Kleinstreuer, Pham, & Sadikot, 2019; Schroeter, Kimbell, Asgharian, Tewksbury, & Singal, 2012; Shang, Dong, Inthavong, & Tu, 2015; Xi, Kim, Si, Corley, & Zhou, 2016). Accordingly, the transport, size change dynamics, and deposition of pure water droplets with initial diameters from 1  $\mu\text{m}$  to 15  $\mu\text{m}$  have been simulated using an experimentally validated CFPD model under resting breathing conditions for both human and rat. Furthermore, the effect of RH and temperature BCs on droplet deposition predictions are quantified by comparing the differences in droplet growth ratio and deposition patterns. For the precise scale-up method, correlations are generated for the regional deposition fractions (DFs) and evaporation fractions (EFs) as functions of Stk/Fr, which unifies rat and human data well on single curves.

## 2. Methodology

### 2.1. Geometry and computational mesh

The human respiratory system configuration (see Fig. 1 (a)) employed in this study was revised based on the geometries used in Zhang, Kleinstreuer, and Feng (2012). The employed human respiratory system has a total surface area of 0.134  $\text{m}^2$ , and it consists of the upper airways (nasal cavity, larynx, and pharynx), trachea, and tracheobronchial (TB) tree from generation 0 (G0) up to G20. Specifically, the upper airway geometry, i.e., from mouth/nose to trachea, was obtained from subject-specific MRI data of a 47-year old healthy male whose body weight was 74 kg (see Fig. 1 (a)). The TB tree was reconstructed with realistic anatomical features using a stochastic algorithm (Kitaoka, 2011). Using Ansys Fluent Meshing 19.2 (Ansys Inc., Canonsburg, PA), the computational domain of the human respiratory system was discretized into 7,064,092 polyhedron based cells. Five near-wall prism layers were generated to resolve the boundary layer and capture laminar-to-turbulence transitions near the walls precisely. It is worth mentioning that the human respiratory system geometry used in this study (see Fig. 1 (a)) is one of the CFPD-ready airway geometries with the capability of predicting anisotropic anatomical pulmonary features to small airways up to G20.

The Sprague-Dawley (SD) rat respiratory system configuration (see Fig. 1 (b)) was kindly provided by Corley et al. (2012). The airway geometry has a total surface area of  $2.72 \times 10^{-3} \text{m}^2$ , which contains a nasal cavity, nasopharynx, trachea, and TB tree from G0 up to G28. The geometry was reconstructed from a 9 to 10-week old SD rat with a bodyweight of 300 g. Employing the same meshing software package, the rat airway was discretized into 11,741,105 polyhedrons plus five near-wall prism layers (see Fig. 1 (b)).

### 2.2. Governing equations

An experimentally validated CFPD model was employed to simulate the transport and deposition of pure-water droplets in human and rat respiratory systems. Based on the assumption that droplets are spherical with negligible droplet-droplet interactions because of the dilute suspension with volume fractions lower than 12%, a one-way coupled Euler-Lagrange based numerical scheme has been employed (Haghnegahdar et al., 2019). The governing equations are provided as follows.

#### 2.2.1. Continuous phase: air and water vapor mixture

Due to the fact that the airflow regime in human and rat respiratory systems are transitional between laminar and turbulence with the resting breathing conditions, the transition shear stress transport (SST) model (Menter et al., 2006) was employed to capture the transition sites with acceptable accuracy. The conservation laws of mass, momentum, turbulence kinetic energy ( $k$ ), and the specific rate of dissipation ( $\omega$ ) are provided in previous studies (Haghnegahdar et al., 2019). Since the mass fraction distributions of water vapor ( $y_w$ ) must be resolved for the accurate prediction of droplet size growth in the respiratory system, the convection-diffusion equation is employed for the calculation of  $y_w$  distribution (Bird, Stewart, & Lightfoot, 1960), i.e.,

$$\frac{\partial(\rho y_w)}{\partial t} + \frac{\partial(\rho u_i y_w)}{\partial x_j} = -\frac{\partial}{\partial x_j} \left( \left( \rho D_w + \frac{\mu_t}{Sc_t} \right) \frac{\partial y_w}{\partial x_j} \right) \quad (1)$$

In this study, air and water are the constituents of the gas mixture. Accordingly,  $\rho$  is the density of the mixture,  $D_w$  is the molecular diffusivity of water in the air,  $\mu_t$  is the turbulent viscosity.  $Sc_t = \mu_t / \rho D_{w,t}$  is the turbulent Schmidt number, and  $D_{w,t}$  is the turbulent diffusivity of water.

Since the temperature distribution is essential for the accuracy of droplet size change dynamics predictions, the conservation of energy was solved too in this study. The energy equation is given as follows (Longest & Xi, 2008):

$$\frac{\partial(\rho c_p T)}{\partial t} + \frac{\partial(\rho u_i c_p T)}{\partial x_j} = \frac{\partial}{\partial x_j} \left[ (k_c + k_{c,t}) \frac{\partial T}{\partial x_j} + h \left( \rho D_w + \frac{\mu_t}{Sc_t} \right) \frac{\partial y_w}{\partial x_j} \right] \quad (2)$$

in which  $c_p$ ,  $T$ ,  $k_c$ , and  $k_{c,t}$  are the specific heat of the gas mixture, temperature, thermal conductivity, and turbulent thermal

conductivity, respectively. In addition,  $h$  is the convective heat transfer coefficient of water. Specifically,  $k_{c,t}$  is defined by:

$$k_{c,t} = \frac{c_p \mu_t}{Pr_t} \quad (3)$$

where  $Pr_t$  is the turbulent Prandtl number defined by:

$$Pr_t = \frac{c_p \mu_t}{k_c} \quad (4)$$

### 2.2.2. Discrete phase: water droplets

The droplets carried by the air-water vapor mixture are subject to multiple forces. To track the trajectory of each droplet, the droplet translation equation (i.e., Newton's 2nd Law) was solved, which can be given as (Haghnegahdar et al., 2019; Hayati, Goharrizi, Salmanzadeh, & Ahmadi, 2019):

$$\frac{d}{dt} (m_p \vec{u}_p) = \frac{1}{8} \pi \rho d_p^2 C_{DP} (\vec{u} - \vec{u}_p) |\vec{u} - \vec{u}_p| + \vec{F}^L + \vec{F}^{BM} + m_p \vec{g} \quad (5)$$

The first term on the right hand side of Eq. (5) is the drag force.  $C_{DP}$  is the drag coefficient (Chen, Feng, Zhong, & Kleinstreuer, 2017).  $F_i^L$  is the Saffman lift force (Saffman, 1965), and  $F_i^{BM}$  is the Brownian motion induced force (Hayati et al., 2019). To capture droplet size change induced by condensation and evaporation, the mass change rate of droplets induced by the evaporative components can be calculated by solving the droplet mass balance equation below (Chen et al., 2017; Longest & Kleinstreuer, 2005):

$$\frac{dm_p}{dt} = - \sum_{s=1}^k \int_{surf} n_s dA_p = - \sum_{s=1}^k (\bar{n}_s A_p) \quad (6)$$

where  $\bar{n}_s$  is the averaged mass flux of evaporative component "s" at the droplet surface. Since water is the only evaporative component in this study, the species index "s" will be replaced by "w" in all the rest equations. Based on the derivation provided by Chen et al. (2017), Eq. (6) can be further rewritten into:

$$\frac{dm_p}{dt} = \frac{Sh D_w C_m}{d_p} A_p \ln \left( \frac{1 - y_{w,\infty}}{1 - y_{w,surf}} \right) \quad (7)$$

In Eq. (7),  $A_p$  is the droplet surface area.  $y_{w,\infty}$  and  $y_{w,surf}$  are the mass fractions of water vapor far from the droplet and at the droplet surface, respectively.  $Sh$  is the Sherwood number, which is given by (Whitaker, 1972):

$$Sh = 2 + \left( 0.4 Re_p^{1/2} + 0.06 Re_p^{2/3} \right) Sc^{0.4} \left( \mu / \mu_{p,surf} \right)^{1/4} \quad (8)$$

where  $\mu$  and  $\mu_{p,surf}$  are the gas mixture viscosities in the far flow field and near droplet surface, respectively. In the present work, the value of  $\mu / \mu_{p,surf}$  is considered 1.0.  $Re_p$  is the droplet Reynolds number.  $Sc = \frac{\mu}{\rho D_w}$  is the Schmidt number.  $C_m$  is the Fuchs-Knudsen number correction, which is defined by (Chen et al., 2017):

$$C_m = \frac{1 + Kn}{1 + \left( \frac{4}{3\alpha_m} + 0.377 \right) Kn + \frac{4}{3\alpha_m} Kn^2} \quad (9)$$

where  $Kn$  is Knudsen number, which is defined by  $Kn = 2\lambda / d_p$ ,  $\lambda$  is the mean free path of water molecules in the air, and  $\alpha_m$  is the mass accommodation coefficient that equals 1.0 (Broday & Georgopoulos, 2001).

At a flat interface between liquid and vapor, the equilibrium vapor pressure and saturation vapor pressure at liquid surface temperature are equal. However, due to the surface curvature effect for small droplets, the equilibrium vapor pressure near the droplet surface is higher than the saturation vapor pressure at surface temperature. Specifically, water molecules can escape from the liquid surface with high curvature easier than from a flat surface, which requires higher vapor pressure to maintain equilibria (Asgharian, 2004; Brechtel & Kreidenweis, 1999). Based on the above-mentioned Kelvin effect, the vapor pressure at equilibrium can be calculated by:

$$K_w = \frac{p_{eq}}{p_{sat}} = \exp \left( \frac{4\sigma \bar{V}_w}{d_p T_p R} \right) \quad (10)$$

where  $p_{eq}$  is equilibrium vapor pressure above the pure liquid droplet,  $p_{sat}$  is the saturation vapor pressure at droplet temperature,  $\sigma$  is droplet surface tension,  $R = 8.314 \text{ J mol}^{-1} \text{ K}^{-1}$  is the gas constant, and  $\bar{V}_w$  is the molar volume of water which is given as (Brechtel & Kreidenweis, 1999):

$$\bar{V}_w = \frac{M_w}{\rho_w} \quad (11)$$

where  $M_w$  denotes the molecular weight of water, and  $\rho_w$  represents droplet density (Kreidenweis et al., 2005). The mass fraction of water vapor at the droplet surface is defined by (Chen et al., 2017; Longest & Hindle, 2012; Longest & Xi, 2008):

$$y_{w,surf} = K_w \frac{P^{sat}}{RT_p} \quad (12)$$

For each droplet, the energy balance equation will also be solved, which is given by:

$$\frac{dT_p}{dt} = \left[ k_{hc} A_p (T - T_p) - \frac{dm_p}{dt} H_{lat} \right] / (m_p c_{p,p}) \quad (13)$$

**Table 1**

Droplet and airflow properties, as well as details of idealized and realistic boundary conditions (BCs).

Droplets Properties			
T (k)	Density (kg/m <sup>3</sup> )		Composition
298.15	993.00		H <sub>2</sub> O
d <sub>p,i</sub> (μm)	Stk/Fr		
	Human	Rat	
1	1.42×10 <sup>-5</sup>	8.36×10 <sup>-5</sup>	
2	-	4.26×10 <sup>-4</sup>	
3	1.92×10 <sup>-4</sup>	-	
4	-	2.28×10 <sup>-3</sup>	
5	6.69×10 <sup>-4</sup>	-	
6	-	6.15×10 <sup>-3</sup>	
7	1.53×10 <sup>-3</sup>	-	
8	-	1.25×10 <sup>-2</sup>	
9	2.85×10 <sup>-3</sup>	-	
11	4.68×10 <sup>-3</sup>	-	
13	7.08×10 <sup>-3</sup>	-	
15	1.01×10 <sup>-2</sup>	-	
Airflow Properties			
T (k)	RH		
298.15	40%		
Realistic BCs			
Regional walls	T (k)	RH (H <sub>2</sub> O mass fraction)	BC type
Nasal cavity	300.15	75% (1.66×10 <sup>-2</sup> )	no slip
Nasopharynx	302.15	75% (1.86×10 <sup>-2</sup> )	no slip
Oropharynx	302.15	75% (1.86×10 <sup>-2</sup> )	no slip
Laryngopharynx	302.15	75% (1.86×10 <sup>-2</sup> )	no slip
Trachea	303.15	75% (1.98×10 <sup>-2</sup> )	no slip
B1	303.15	75% (1.98×10 <sup>-2</sup> )	no slip
B21, B22	305.15	83% (2.46×10 <sup>-2</sup> )	no slip
LUL, LLL, RUL, RML, RLL	310.15	99.5% (3.92×10 <sup>-2</sup> )	no slip
Idealized BCs			
Region	T (k)	RH (H <sub>2</sub> O mass fraction)	BC type
Nasal inlets	298.15	40% (7.80×10 <sup>-3</sup> )	velocity inlet
Walls	310.15	99.5% (3.92×10 <sup>-2</sup> )	no slip
Outlets	310.15	99.5% (3.92×10 <sup>-2</sup> )	pressure outlet

Here  $T_p$  and  $c_{p,p}$  are the temperature and specific heat of droplet.  $k_{hc}$  is the modified thermal conductivity, which can be calculated by:

$$k_{hc} = k_{mc} \frac{Nu k_c}{Sh D_w} \quad (14)$$

where  $k_c$  is the thermal conductivity of the gas mixture, and  $Nu$  is the Nusselt number. In addition,  $k_{mc}$  is the mass transfer coefficient, which is defined as  $k_{mc} = C_m D_w Sh / d_p$ . Assuming the droplets have a uniform spatial temperature distribution and there is no internal resistance to heat transfer,  $Nu$  can be defined by (Whitaker, 1972):

$$Nu = 2 + \left( 0.4 Re_p^{1/2} + 0.06 Re_p^{2/3} \right) Pr^{0.4} \left( \mu / \mu_{p,surf} \right)^{1/4} \quad (15)$$

### 2.3. Numerical setup

Ansys Fluent 19.2 (Ansys Inc., Canonsburg, PA) was used for the CFPD simulations. The flow time step is 0.02 s, which is determined by the time step independence test. The first breathing cycle with a realistic breathing pattern through nostrils (Haghnegahdar et al., 2019) was simulated without droplet inhalation (please see Fig. 3 for the breathing waveforms). During the second breathing cycle, droplets with different initial diameters (1  $\mu\text{m}$ , 3  $\mu\text{m}$ , 5  $\mu\text{m}$ , 7  $\mu\text{m}$ , 9  $\mu\text{m}$ , 11  $\mu\text{m}$ , 13  $\mu\text{m}$ , and 15  $\mu\text{m}$ ) were injected at 8 different time stations into the human human respiratory system between  $t = 4$  s (i.e., the beginning of the second breathing cycle) and  $t = 4.3$  s. Droplets with different initial diameters (1  $\mu\text{m}$ , 2  $\mu\text{m}$ , 4  $\mu\text{m}$ , 6  $\mu\text{m}$ , and 8  $\mu\text{m}$ ) were injected at 6 different time stations into the rat respiratory system between  $t = 0.6$  s to  $t = 0.74$  s (the first 6 time steps before reaching the inhalation peak) with an idealized sinusoidal breathing waveform mimicking rat breathing at rest (Corley et al., 2015) (see Fig. 3). The range of initial diameters ( $d_{p,i}$ ) was selected based on their corresponding inlet  $Stk/Fr$  based on the mean inlet velocity of the inhalation phase. The physical properties of humid airflow and droplets are listed in Table 1 (Haghnegahdar et al., 2019). For both models, the more realistic RH and temperature BCs were obtained from (Ferron et al., 2013) and employed (see Table 1 for details).

Additionally, in-house user-defined functions (UDFs) were developed and compiled for:

- (1) Specifying transient inhalation and exhalation profiles at the nostrils;
- (2) Recovering the anisotropic corrections on turbulence fluctuation velocities;
- (3) Modeling the Brownian motion induced forces;
- (4) Calculating droplet size change due to the evaporation and condensation; and
- (5) Storing droplet deposition data.

Numerical simulations were performed on a local Dell Precision T7810 workstation (Intel® Xeon® Processor E5-2643 v4 with dual processors, 64 cores and 128 GB RAM) and a local Dell Precision T7910 workstation (Intel® Xeon® Processor E5-2683 v4 with dual processors, 64 cores, and 256 GB RAM). Using 32 cores, it took approximately 28 hours (particles of  $d_{p,i} = 15 \mu\text{m}$  for human airway) to 11 hours (particles with  $d_{p,i} = 1 \mu\text{m}$  for rat airway) to complete one simulation.

### 2.4. Model validation

The current CFPD model was validated in earlier studies by comparing the airflow field and hygroscopic droplet transport and

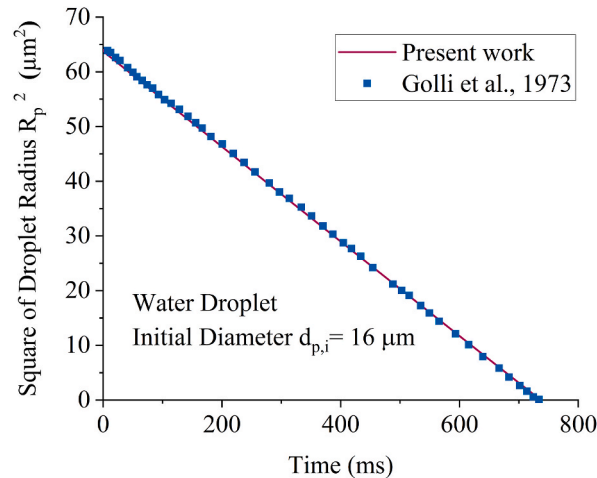


Fig. 2. CFPD model validations on the prediction of size change dynamics of pure water droplets.

deposition with benchmark experimental data (Haghnegahdar et al., 2018; A. Haghnegahdar et al., 2019; Zhang et al., 2012). To validate the capability of predicting pure-water droplet size change, numerical results using the CFPD model in this study were compared with the experimental data (Golli, Arnaud, Bricard, & Treiner, 1977). Specifically, droplets with initial diameter  $d_{p,i} = 16 \mu\text{m}$  were simulated with ambient  $\text{RH} = 70\%$ . The humid airflow velocity at the square channel's inlet (see Fig. 2) is 0.12 m/s. The size change over time predicted by the CFPD model and measured by experiments (Golli et al., 1977) are both shown in Fig. 2. Good agreement can be observed between the numerical prediction and experimental data, which demonstrates the CFPD model's reliability in predicting the condensation and evaporation between pure water droplets and ambient humid air.

### 3. Results and discussion

#### 3.1. Pulmonary airflow fields

Figures 3 (a) and (b) visualize the distributions of the normalized velocity ( $V^*$ ) of the air-water vapor mixture in human and rat nasal cavities at the inhalation peak flow rates (see breathing waveforms in Figs. 3 (a) and (b)).  $V^*$  is defined as the ratio between the local velocity magnitude and the time-averaged inlet velocity during inhalation. In the human nasal cavity, the airflow inhaled from nostrils experiences a mild turn after reaching the nasal valve, resulting in an increase of  $V^*$  to 1.6. In the rat nasal cavity, sharper turns can be observed near the nasal vestibule. These abrupt changes in airflow directions lead to a highly skewed velocity distribution, which increases the localized  $V^*$  up to 6.4. Because of the curvature of the nasal passage centerline, the centrifugal force also has high velocity near the front nasal cavities for both the human and the rat. Such a skewed velocity distribution also results in localized flow recirculation locally in the human nasal cavity. The value of  $V^*$  in the rat anterior nose (relative to that in the human anterior nose) drops faster, because the size of the human nasal cavity is considerably larger than that of the rat. The maximum  $V^*$  decreases from 1.6 to 1.3 from the nasal valve to the nose anterior in humans (see Fig. 3 (a)), whereas it drops from 6.4 to 1.5 in the rat nose (see Fig. 3 (b)).

Furthermore, the airflow fields in the extrathoracic regions of both human and rat at the time stations with the peak inhalation flow rates (see Figs. 3 (a) and (b)) are shown in Figs. 4 (a) and (b). The streamlines shown in Fig. 4 (a) indicate the mainstream transport

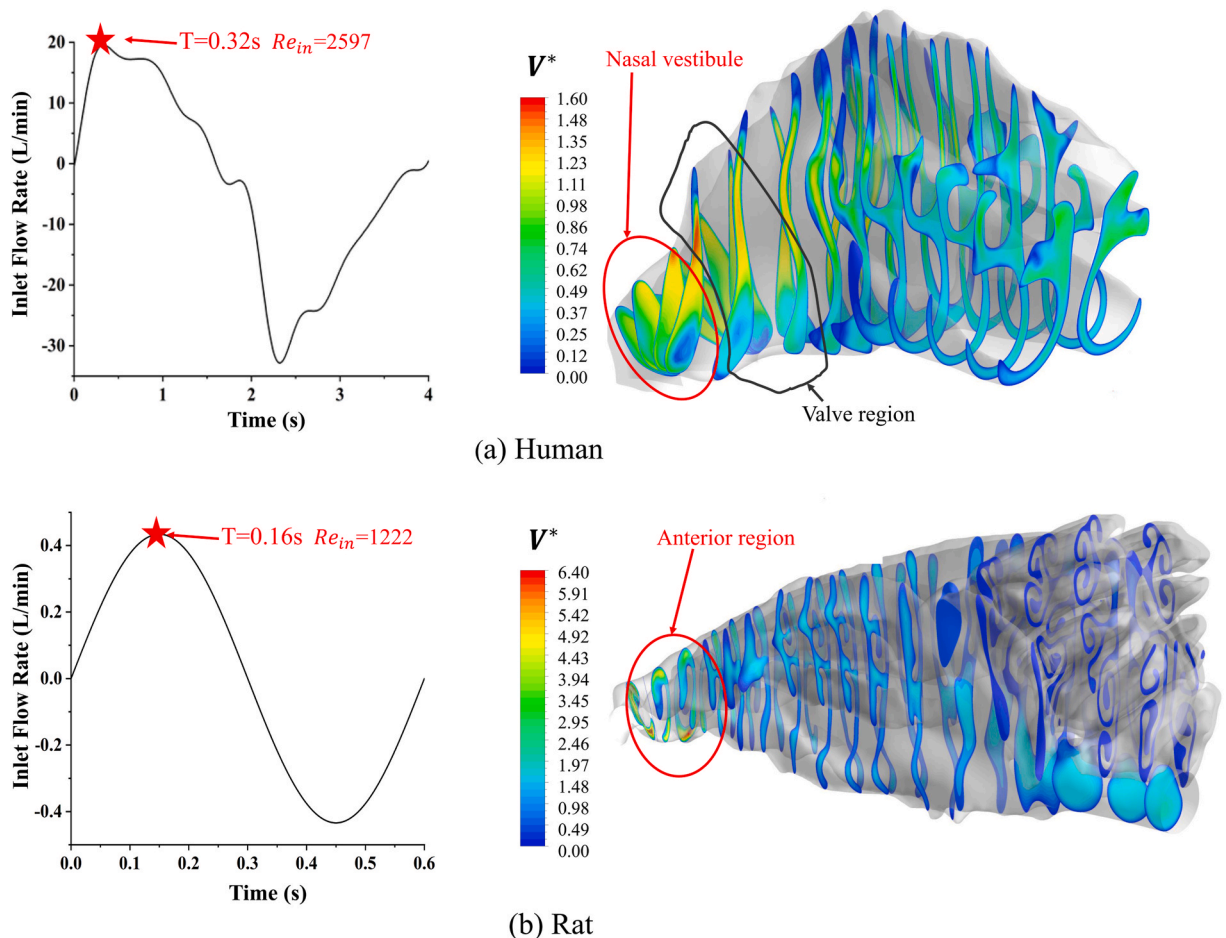


Fig. 3. Distributions of normalized velocity magnitude  $V^*$  in nasal cavities at peak inhalation flow rates: (a) human, (b) rat.

through the entire human nasal cavity, but predominantly through the respiratory region. Specifically, the mainstream of airflow is transported toward the middle meatus, while only a small portion of the airflow transports toward the inferior meatus, followed by continuous swirling and detachment from the walls. The olfactory region and superior meatus have the lowest number of streamlines in the human nasal cavity. With the streamline distributions shown in Fig. 4 (a), the strong impaction of the airflow in the nasal cavity and the secondary flow-induced interception are the two main deposition mechanisms for inhaled droplets, which are discussed in detail in Section 3.3. In the human nasopharynx, the velocity distribution is highly asymmetric because of the asymmetric anatomical airway shape and the non-uniform upstream flow distributions in the nasal cavity (see cross-section N–N' in Fig. 4 (a)). The secondary flow in cross-section N–N' indicated by the in-plane velocity vectors shows the quasi double-vortex structure. Specifically, the two vortices shown in N–N' rotate in opposite directions, which is determined by the lower pressure near the center of N–N' due to the high velocity in the airflow mainstream. It is interesting to notice that airflow circulations can enter the oral cavity, although the mouth is closed (see the streamlines shown in Fig. 4 (a)). As a result, the airflow that enters the oral cavity can also carry droplets and result in a deposition in that area. When flow passes the larynx, the high-velocity laryngeal jet is generated. Secondary flows and non-uniform velocity distributions are visualized at cross-sections O–O', L1–L1', L2–L2', and L3–L3'. Because of the pressure difference between the main flow and the flow adjacent to the larynx anterior, swirling happens. Some of the flow streamlines leave the bulk and move toward the wall while their velocity decreases. Comparatively, Fig. 4 (b) visualizes the flow streamlines in the extrathoracic region of the rat airways. The velocity increases considerably because the cross-sections perpendicular to the mainstream direction are smaller than those of nostrils. After passing the nasal vestibule, the airflow is also distributed unevenly in the nasal cavity. Specifically, the streamlines entering the respiratory region from the anterior nose directly exit the nasal cavity and enter the pharynx. A significant portion of the inhaled airflow passes turbinate and reaches the trachea directly without entering the olfactory region (see Fig. 4 (b)). The small portion of airflow entering the olfactory region has relatively low velocity. In addition, on cross-section P1–P1' the secondary flow is directed toward the anterior wall near P1'. With the decreases in the lumen at cross-sections P2–P2' and P3–P3', the high-velocity laryngeal jet is formed close to the superior wall of the trachea. With the smaller opening of cross-section L1–L1' (i.e., the rat glottis), the high-velocity glottis jet is generated and extends through cross-section L2–L2'. Therefore, Figs. 4 (a) and (b) indicate that there are distinguished airflow patterns in human and rat extrathoracic regions due to the anatomical differences, which can lead to droplet depositions that will not be proportional to the airway surface areas.

Figure 5 shows the normalized velocity magnitude  $V^*$  contours at representative cross-sections in different generations of TB trees for both human and rat (see Fig. 1 for the locations of selected cross-sections). It can be observed that the velocity distributions in the representative cross-sections from G0 to G16 are highly non-axisymmetric in both human and rat TB trees. Such non-axisymmetric velocity contours are due to the relatively higher local Reynolds number, leading to the un-fully developed flow patterns in the airways with high curvature and the near bifurcating point. In addition, the secondary flow patterns are shown by the in-plane velocity vectors in all cross-sections.  $V^*$  is higher in the rat TB than human TB, which is mainly because of the much narrower airway lumen in the rat lung than the human lung. The developing velocity profiles in selected cross-sections from G0 to G16 indicate that it is necessary to cover the entire 3D airways from G0 to G16 to accurately describe the anisotropic airflow fields in any whole-lung model reconstructions. Simplifications to one dimensional (1D) network in G0–G16 may result in inaccurate predictions of pulmonary airflow field and particle transport dynamics. In contrast, Fig. 5 also shows that airflow velocity distributions become quasi fully developed from G17 to G20 in the human respiratory system and from G21 to G28 in the rat respiratory system. Specifically, the quasi fully developed velocity profiles are parabolic. Such observations imply the negligible secondary flows starting from G17 in human airway and G28 in rat airway models. Therefore, it is feasible to employ truncated airway models or 1D network models to capture the mainstream flow characteristics in G17 and beyond the human whole-lung model and G21 and beyond in the rat whole-lung model to optimize the computational cost without losing precision.

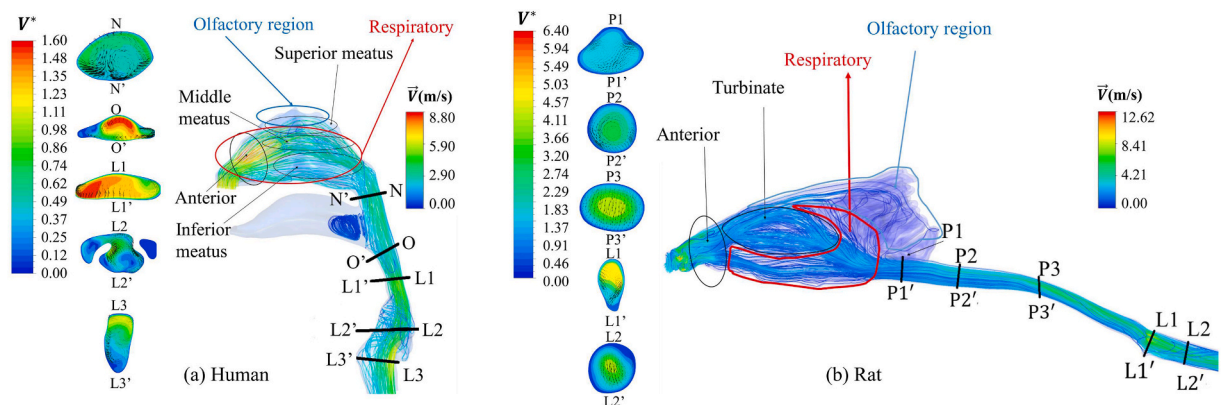


Fig. 4. Streamlines, normalized velocity magnitude  $V^*$  contours, and in-plane velocity vector distributions in extrathoracic regions at peak inhalation flow rates: (a) Human and (b) Rat.

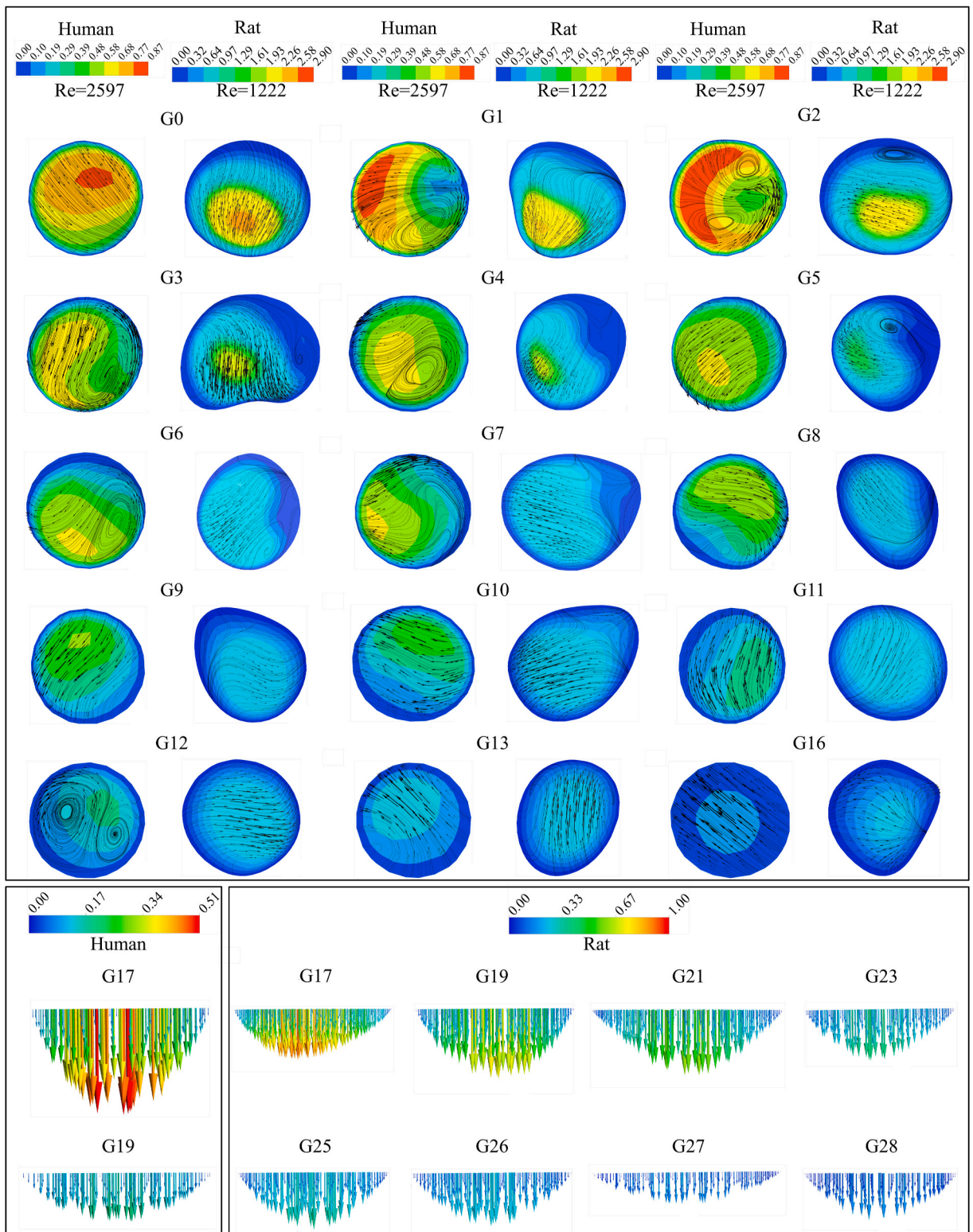


Fig. 5. Normalized velocity magnitude  $V^*$  distributions at cross-sections in different generations of the human and rat respiratory systems at peak inhalation flow rates.

### 3.2. Relative humidity (RH) distribution

Figures 6 (a)-(d) show RH on randomly selected lines in different pulmonary regions at the inhalation peak flow rate (see the breathing waveforms in Fig. 3) in both human and rat respiratory systems. As shown in Fig. 6 (a), the average RH gradually increases from the nostril into the nasal cavity along the nasal passages. Such a phenomenon is because the inhaled dry air is mixed with the high-humidity air near the nasal airway walls during the transport. It can also be observed in Fig. 6 (a) that the minimum RH rises considerably from around 0.45 to around 0.67 from the nasal cavity to the nasopharynx. Affected by the asymmetric velocity field, RH distribution is also asymmetric to the cross-sectional lines. Influenced more by the high humidity at the airway walls, the inhaled airflow becomes more saturated from the larynx to the deeper TB tree, which can be observed from the higher and more evenly distributed RH profiles from G3 to G17 (see Fig. 6 (b)). It can be observed from Fig. 6 (b) that RH distribution does not become uniform and saturated in the airways higher than G17. In comparison, Figs. 6 (c) and (d) show that the RH of inhaled airflow reaches the maximum value in the nasal cavity at the downstream location near vestibule, i.e., 0.75, which is the same RH at the nasal cavity wall. The quick absorption of the humidity is because of the larger surface-area-to-volume ratio of the rat nasal cavity compared to the human nasal cavity. Specifically, the larger surface-area-to-volume ratio of the rat nasal cavity will lead to a more substantial influence by the high-humidity nasal wall boundary condition, resulting in faster humidity absorption. Furthermore, Fig. 6 (d) shows that the RH distribution becomes more evenly distributed and increases to 0.995 from G4 to G13. The airflow becomes saturated at G13.

### 3.3. Transport, size change, and deposition of the inhaled water droplets

Using the more realistic RH and temperature boundary conditions (see the realistic BCs presented in Table 1), the transport, size change dynamics, and deposition patterns of the inhaled water droplets are visualized in Figs. 7–9. It worth mentioning that, based on the statistics of droplet fates in all simulations, droplets all deposited or evaporated in both human and rat respiratory systems during the inhalation-exhalation processes.

In Figs. 7 (a) and (b), the growth ratio (GR) of deposited droplets in the human and rat airways are plotted, which are colored by their initial diameters  $d_{p,i}$ . Specifically, GR is defined by:

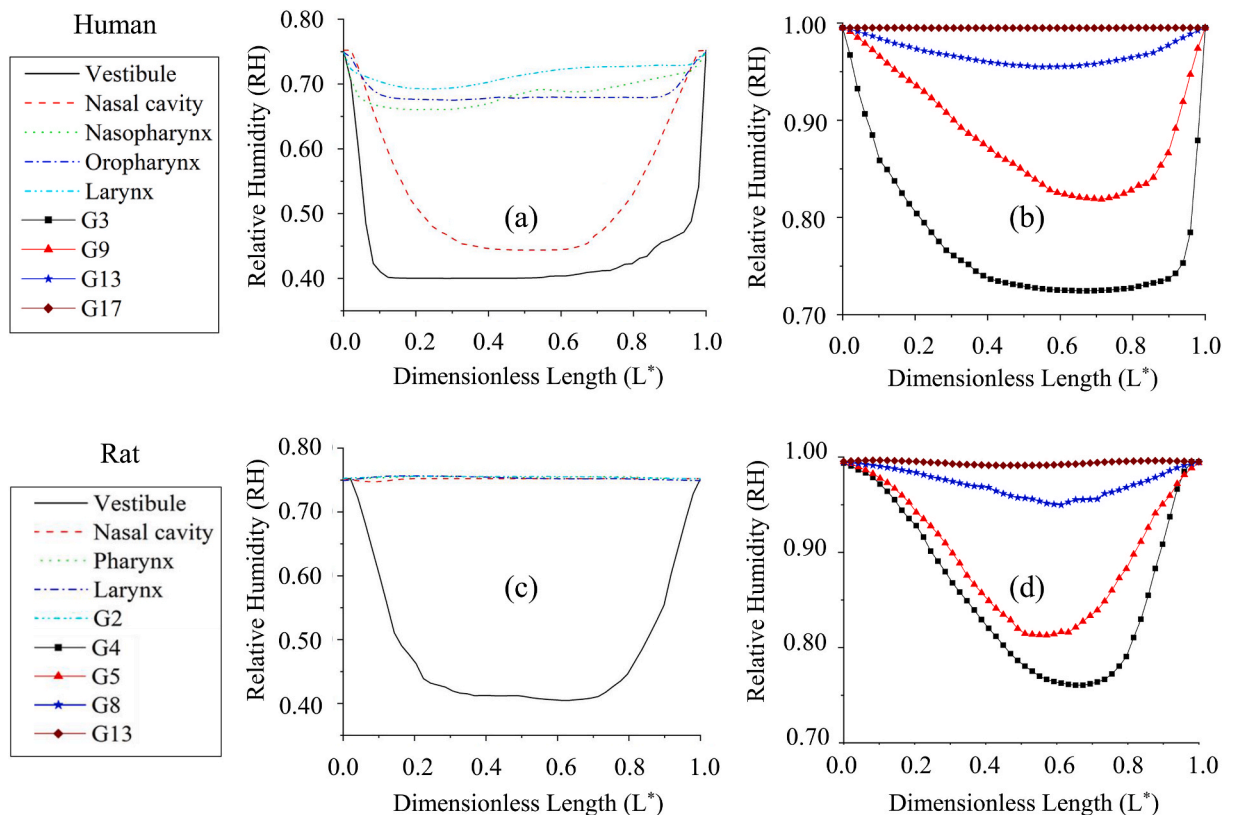
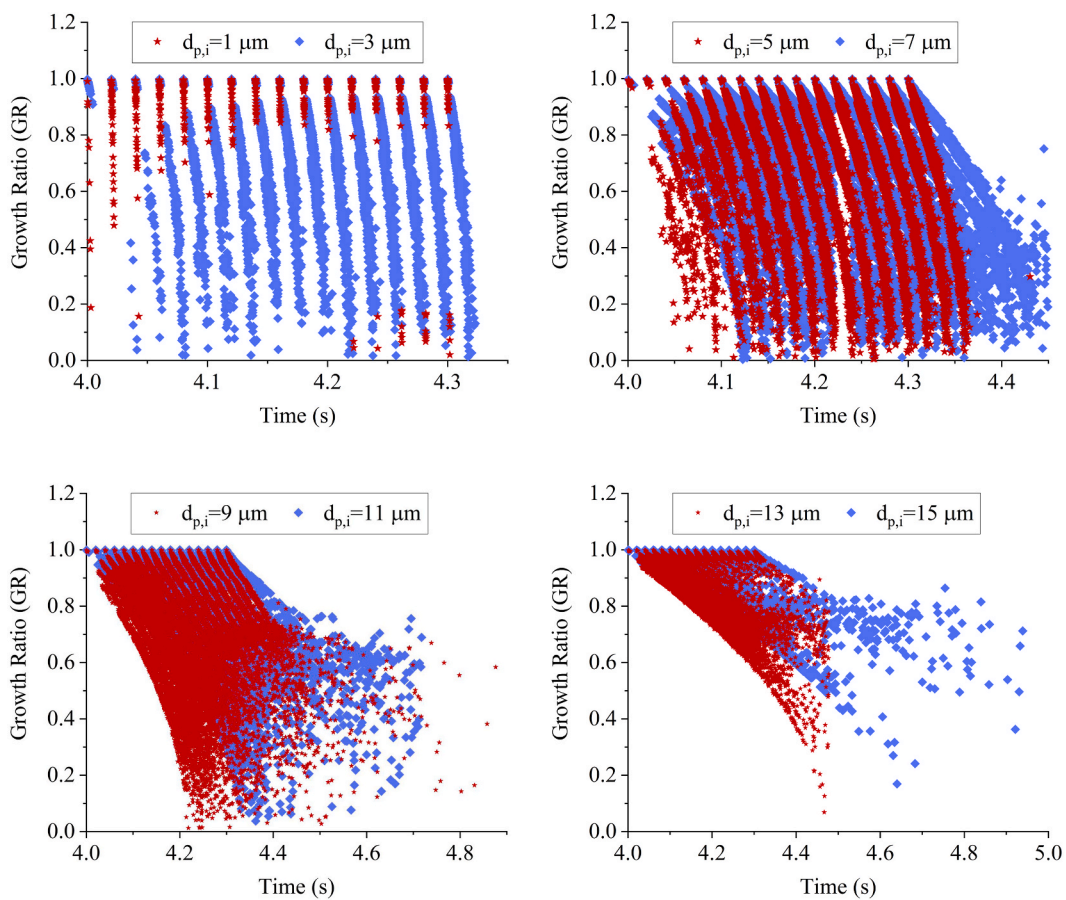
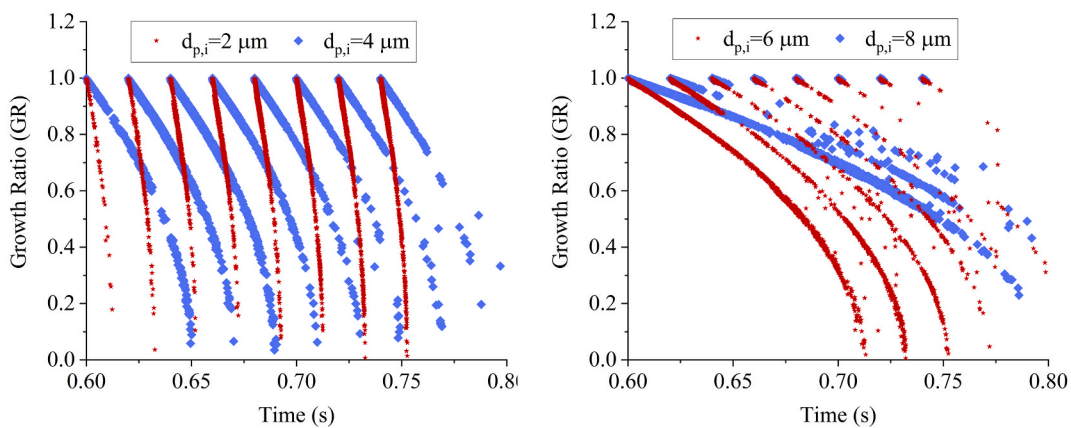


**Fig. 6.** Relative humidity (RH) distributions in respiratory systems under realistic BCs at the peak inhalation flow rates: (a) selected locations in the human upper airway, (b) selected locations in the human tracheobronchial (TB) tree, (c) selected locations in the rat upper airway, and (d) selected locations in the rat tracheobronchial (TB) tree.



(a) Human



(b) Rat

Fig. 7. Growth ratios ( $GR = d_{p,f}/d_{p,i}$ ) of deposited droplets under realistic BCs: (a) human, and (b) rat.

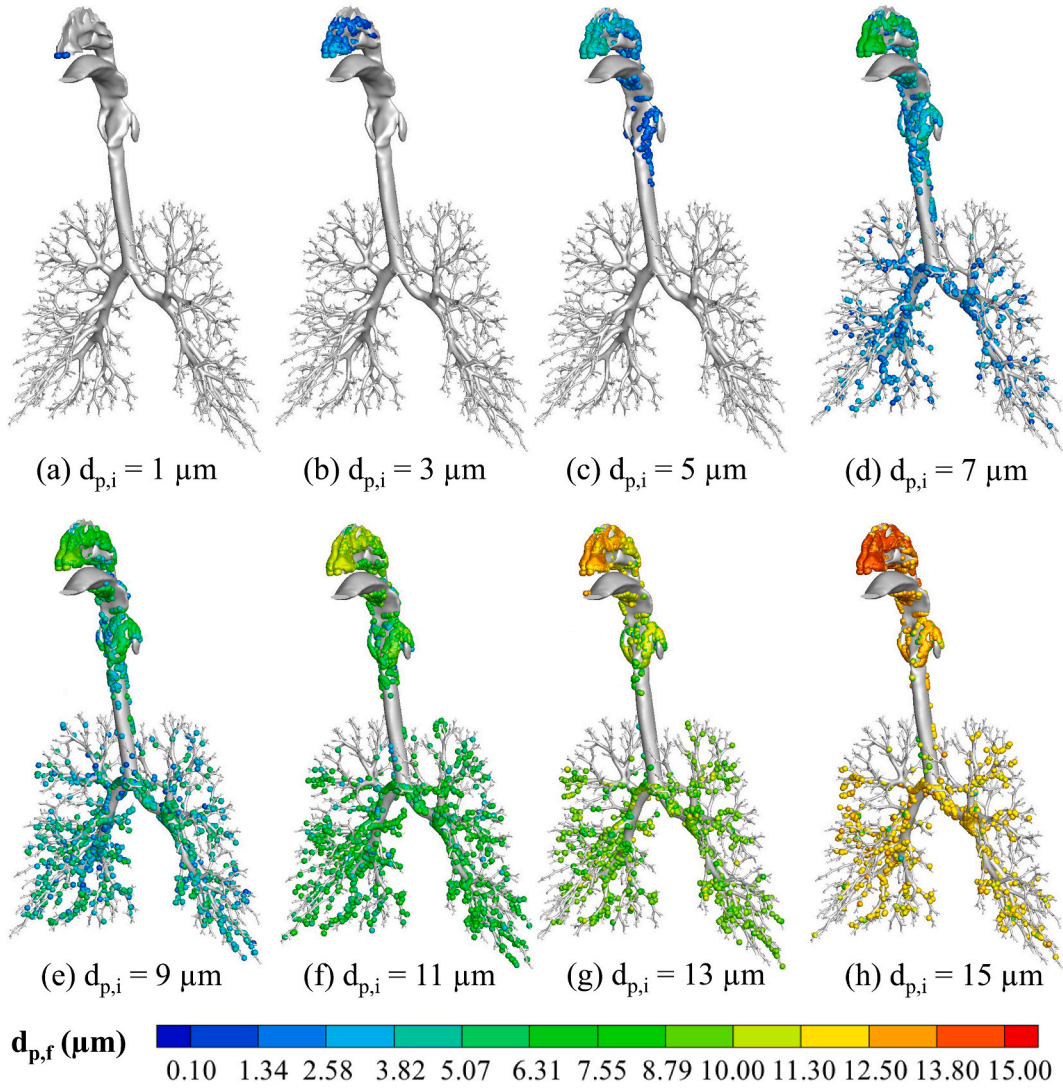


**Fig. 8.** Droplet deposition patterns with different initial diameters in the human respiratory system under realistic BCs: (a)  $d_{p,i} = 1 \mu\text{m}$ , (b)  $d_{p,i} = 3 \mu\text{m}$ , (c)  $d_{p,i} = 5 \mu\text{m}$ , (d)  $d_{p,i} = 7 \mu\text{m}$ , (e)  $d_{p,i} = 9 \mu\text{m}$ , (f)  $d_{p,i} = 11 \mu\text{m}$ , (g)  $d_{p,i} = 13 \mu\text{m}$ , (h)  $d_{p,i} = 15 \mu\text{m}$ .

$$GR = \frac{d_{p,f}}{d_{p,i}} \quad (16)$$

Under the realistic BCs shown in Table 1, the water mass fraction  $y_{w,\infty}$  in the humid airflow is less than 0.04, while the water mass fraction near the droplet surface  $y_{w,surf}$  is at the saturation point, which is constantly higher. Therefore, the average diameters of droplets deposited later in the human respiratory systems (see Fig. 7 (a)) is smaller than droplets deposited earlier due to the continuous water evaporation. Additionally, since the initial droplet temperature (298.15 K) is lower than the wall temperatures in the human respiratory system (from 300.15 K to 310.15 K), no condensation induced hygroscopic growths are noticed for inhaled pure water droplets. It can also be observed from Fig. 7 (a) that droplets with smaller initial sizes evaporate faster than larger droplets, i.e.,  $1 \mu\text{m}$  vs.  $3 \mu\text{m}$ ,  $5 \mu\text{m}$  vs.  $7 \mu\text{m}$ ,  $9 \mu\text{m}$  vs.  $11 \mu\text{m}$ , and  $13 \mu\text{m}$  vs.  $15 \mu\text{m}$ . The same  $d_{p,i}$  effect on droplet growth ratio is also found in the rat respiratory system (see Fig. 7 (b)). Specifically, Droplets with  $d_{p,i} = 2 \mu\text{m}$  and  $d_{p,i} = 6 \mu\text{m}$  decrease in their size at a higher rate compared with those with  $d_{p,i} = 4 \mu\text{m}$  and  $d_{p,i} = 8 \mu\text{m}$ , respectively. The trends mentioned above are because in the continuum limit, the change in droplet diameter is inversely proportional to droplet diameter for condensation and evaporation. Another interesting finding is that GR ranges are wider for deposited droplets with  $d_{p,i} = 3 \mu\text{m}$  compared with  $d_{p,i} = 1 \mu\text{m}$  at the same time station (see Fig. 7 (a)). It is because that a large portion of droplets with  $d_{p,i} = 1 \mu\text{m}$  totally evaporate before they can deposit on airway walls due to their faster evaporation rate than droplets with larger initial sizes.

With the realistic BCs, localized droplet deposition patterns in human and rat airways are presented in Figs. 8 and 9, respectively. Droplets are colored by their final diameter  $d_{p,f}$ . As observed in Fig. 3 (a), inhaled airflow in the human nasal cavity experiences

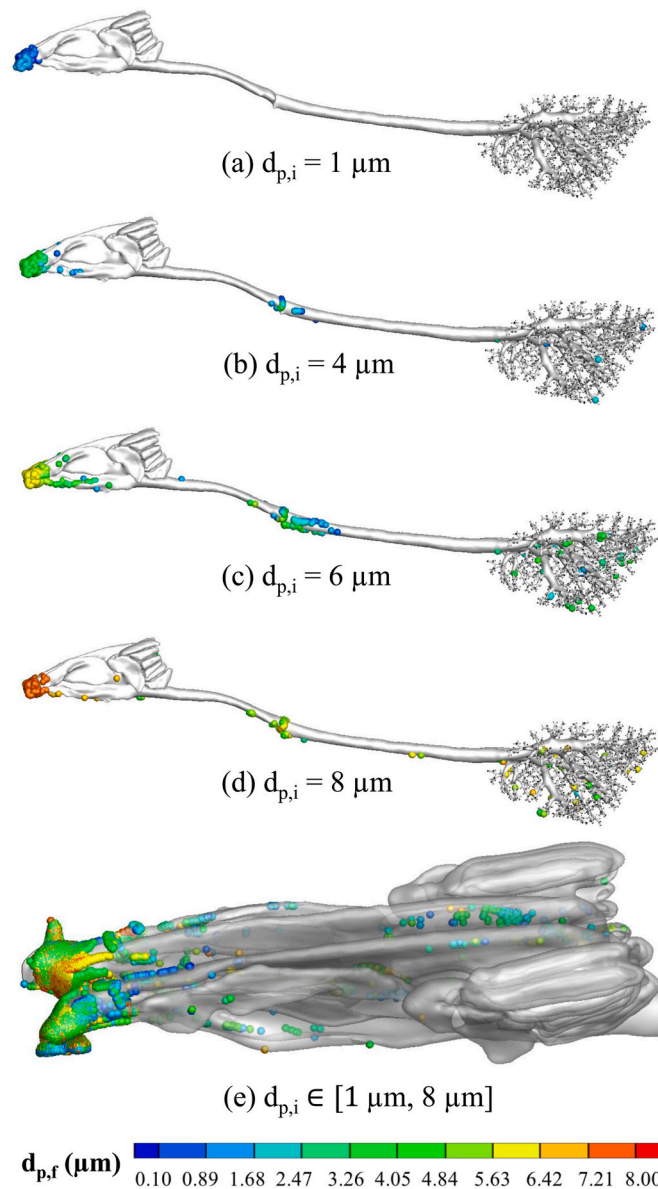


**Fig. 9.** Droplet deposition patterns in the rat respiratory system under realistic BCs: (a)  $d_{p,i} = 1 \mu\text{m}$ , (b)  $d_{p,i} = 4 \mu\text{m}$ , (c)  $d_{p,i} = 6 \mu\text{m}$ , (d)  $d_{p,i} = 8 \mu\text{m}$ , (e)  $d_{p,i} \in [1 \mu\text{m}, 8 \mu\text{m}]$ .

continuous direction changes, which lead to inertial impactions of the carried droplets. Accordingly, with the increase in droplet initial diameters, the deposition due to the inertial impaction in the anterior of the human nasal cavity also increased (see Figs. 8 (a)-(h)). It is worth mentioning that most of the droplets with  $d_{p,i} = 1 \mu\text{m}$  evaporate shortly after they enter the nasal cavity, which is why the droplet depositions are scattered only near the nasal vestibule in Fig. 8 (a). As the initial size of the droplets increases, they can stay in the domain longer due to the longer time to fully evaporate. The droplets color in Fig. 8 (a)-(h) indicates that their size reduces their transport, so they are able to become less influenced by the inertial impaction and gravitational sedimentation and can follow the mainstream of the airflow into the deeper airways. For example, droplets with  $d_{p,i} = 3 \mu\text{m}$  (see Fig. 8 (b)) can reach deeper parts of the nasal cavity compared to those with  $d_{p,i} = 1 \mu\text{m}$  (see Fig. 8 (a)). With the low airflow velocity and convection effect in the olfactory region (see Fig. 4 (a)), 3- $\mu\text{m}$  droplets suspended in this region and continuously reduce in size and will be totally evaporated before entering the nasopharynx. In contrast, droplets with larger initial diameters, e.g.,  $d_{p,i} = 5 \mu\text{m}$ , will be able to remain in the airway as discrete droplets and reach the mid of the trachea (see Fig. 8 (c)). Figure 8 (c) shows that concentrated deposition sites are the nasopharynx, the lower oropharynx, and the anterior wall of the larynx, due to the combined influence of high-velocity jet impaction and the interception of the recirculated airflow patterns shown in Fig. 4 (a). Droplets with  $d_{p,i} \geq 7 \mu\text{m}$  can reach the deepest part of the human respiratory system (see Figs. 8 (d)-(h)). With the continuous reduction in droplet sizes, the deposition patterns in the TB tree for

droplets with  $d_{p,i} \geq 7 \mu\text{m}$  are more evenly distributed. Compared to the concentrated deposition patterns in the upper airway, which is dominated by inertial impaction and gravitational sedimentation, droplets deposited in the TB trees are smaller in diameter, which will be dominated by turbulence dispersion.

For droplet depositions in the rat respiratory system (see Figs. 9 (a)-(e)), a similar initial diameter effect on deposition patterns can be observed in the rat airways compared with the human airways (see Figs. 8 (a)-(h)). Specifically, the larger the  $d_{p,i}$  is, the more the droplets can penetrate into the lower airways before totally evaporating. The deposition of droplets with  $d_{p,i} = 1 \mu\text{m}$  only can be found in the nasal vestibule (see Fig. 9 (a)) since most of them evaporate completely before deposition. In contrast, most of the droplets with  $d_{p,i} = 4 \mu\text{m}$  are found deposited in both the nasal vestibule and near the glottis (see Fig. 9 (b)). A small amount of those droplets deposits in the rat TB tree. With the further increase in  $d_{p,i}$ , i.e.,  $d_{p,i} = 6 \mu\text{m}$  (see Fig. 9 (c)), more droplets can escape complete evaporation in the airway so that more can transport further and be deposited in TB trees. In the larynx, the secondary flow is toward the anterior wall that can affect droplet deposition. Deposition of droplets with  $d_{p,i} = 4 \mu\text{m}$  and  $6 \mu\text{m}$  in the larynx can be affected mostly by secondary flow and dispersion with their final size ranges from  $0.01 \mu\text{m}$  to  $4 \mu\text{m}$ . Interestingly, the deposition pattern changes in a nonmonotonic style with the further increase  $d_{p,i}$  (see Fig. 9 (d)). Indeed, droplets with  $d_{p,i} = 8 \mu\text{m}$  mostly deposit in the nasal vestibule because of inertial impaction, and a few of them will reach the trachea and lower airway because their sizes are still too large to avoid the inertial impaction and gravitation sedimentation in upper rat airways. Figure 9 (e) compares deposition patterns for droplets with different  $d_{p,i}$  in the rat nasal cavity (top view). It can be seen that most droplets deposit at the anterior region of the rat nasal cavity, and only a few droplets can deposit in the olfactory and turbinate regions. Such an observation indicates that using the nose cones for rats to inhale toxic aerosols may not be efficient for investigating the health risks to their pulmonary system since most of the micro-sized aerosol droplets may not be able to enter the TB tree. The deposition pattern in the rat nasal cavity (see Fig. 9 (e)) is determined by multiple deposition mechanisms. Both posterior and anterior areas of the pharynx are covered by droplets caused by the effects of gravity, diffusion, secondary flow, and inertia (see cross-sections P1–P1', P2–P2', and P3–P3' in Fig. 3 (b)).

In summary, the comparisons of the droplet sizes and deposition patterns between human and rat respiratory systems demonstrate that the differences in airway anatomy and RH and temperature distributions between human and rat will significantly influence the

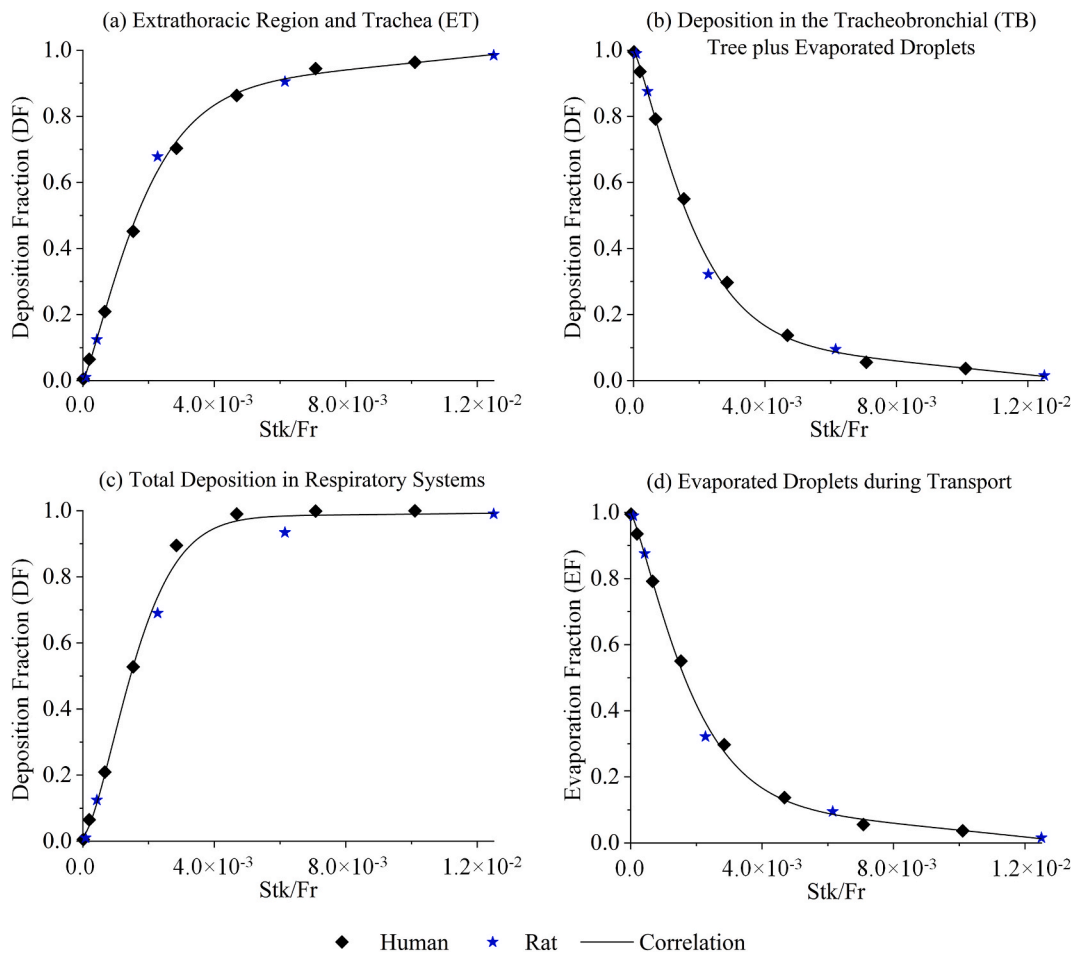


Fig. 10. Aligned deposition fractions (DFs) and evaporation fraction (EF) in both human and rat respiratory systems as a function of Stk/Fr: (a) DF in ET, (b) DF in TB plus EF, (c) total DF in respiratory systems, and (d) EF of droplets during transport.

droplet fates and must be considered for a precise scale-up method. Accordingly, by introducing dimensionless number group  $Stk/Fr$  in Section 3.4, a new scale-up correlation is proposed, which contains the inter-species variabilities in many aspects mentioned above.

### 3.4. Deposition fraction (DF) and evaporation fraction (EF) vs. $stk/fr$

To find unified correlations to estimate droplet depositions in both human and rat airways, deposition fractions (DFs) in multiple regions and evaporation fraction (EF) of droplets are plotted as functions of droplet  $Stk/Fr$  at the inlets. Specifically, Stokes number ( $Stk$ ) and droplet Froude number ( $Fr$ ) are defined as:

$$\frac{Stk}{Fr} = \frac{\rho_w d_{p,i}^2 v \sqrt{g d_{p,i}}}{18\mu D_{in} v} = \frac{\rho d_{p,i}^{2.5} g^{0.5}}{18\mu D_{in}} \quad (17)$$

Specifically,  $Stk$  is a dimensionless number indicating the relative importance between inertial forces and viscous forces acting on the particles. At the same time,  $Fr$  is a dimensionless number measuring the ratio of importance between the inertial impaction and gravitational sedimentation effects on particle depositions. Accordingly,  $Stk/Fr$  focuses on the relative importance of gravitational effect and inertial impaction vs. viscous effects on particle transport dynamics. It is a good indicator of the relative dominancy of inertial impaction and gravitational sedimentation on particle deposition. After many attempts of using multiple combinations of dimensionless numbers, it was found that using  $Stk/Fr$  can make the lung deposition data in both human and rat respiratory systems align with the same curves. Such findings indicate that if  $Stk/Fr$  number is identical for the particles inhaled by human and rat, the deposition fractions (DFs) in certain airway regions of the human and the rat respiratory systems are very similar (see Fig. 10 (a)-(d)), which are mostly independent of the geometric features employed in this study. High  $Stk/Fr$  indicates that the gravitational effect and inertial impaction are more dominant than the viscous dissipation effect. Compared with the dimensionless groups used in existing studies (Calmet et al., 2018; Xi et al., 2016), using  $Stk/Fr$  can encompass the three dominant mechanisms mentioned above that can influence the particle transport and deposition, i.e., breathing at rest through noses, for both human and rat. Detailed analysis is discussed as follows.

Figures 10 (a)-(d) visualize the regional DFs, total DFs, and EFs in both human and rat respiratory systems as a function of droplet  $Stk/Fr$  with different initial diameters. It can be observed from Figs. 10 (a), (b), and (d) that DFs in the extrathoracic regions and tracheas ( $DF_{ET}$ ), DFs in the entire TB trees ( $DF_{TB}$ ) plus EFs, and EFs during the droplet transport in both human and rat align well with single curves. The total DFs shown in Fig. 10 (c) are aligned with a single curve well, except for the noticeable deviation found for DF in the rat respiratory system for droplets with  $Stk/Fr = 0.00615$ . Based on the unified curves shown in Figs. 10 (a)-(d), increasing  $Stk/Fr$  can enhance the deposition in the extrathoracic region and trachea ( $DF_{ET}$ ) and the total depositions for both human and rat. To provide a unified function for estimating the depositions for both human and rat under resting breathing conditions (see Fig. 3), the nonlinear least-square method is used for the curve fitting, which generates a correlation for  $DF_{ET}$  in terms of  $Stk/Fr$  (see Fig. 10 (a)), i.e.,

$$DF_{ET} = C_1 \exp\left(C_2 \frac{Stk^{C_3}}{Fr}\right) + C_4 \exp\left(C_5 \frac{Stk^{C_3}}{Fr}\right) \quad 1.42 \times 10^{-5} \leq \frac{Stk}{Fr} \leq 0.0125 \quad (18)$$

Values of  $C_i$  ( $i = 1, 2, 3, 4, 5$ ) are provided in Table 1. Since no droplets were found exhaled from the nostril, the summation of the DF in the entire TB trees ( $DF_{TB}$ ) and the evaporated droplet fractions (EF) (see Fig. 10 (b)) can be estimated by:

$$DF_L = DF_{TB} + EF = 1 - DF_{ET} \quad (19)$$

Using the same form of the correlation in Eq. (18) with different coefficient values, the total depositions shown in Fig. 10 (c) can also be estimated. The updated values of  $C_i$  ( $i = 1, 2, 3, 4, 5$ ) are also provided in Table 2. It worth mentioning that the mean square deviations (MSDs) of Eq. (18) were calculated for the evaluation of how well the correlations can represent deposition fractions shown in Figs. 10 (a) and (c). Specifically, MSDs were computed using the following equation:

$$MSD = \frac{1}{n} \sum_{i=1}^n (DF_i - \widehat{DF}_i)^2 \quad (20)$$

where  $\widehat{DF}_i$  is the deposition fraction estimated using Eq. (18), and  $DF_i$  is obtained from CFPD simulation results, and  $n$  is the number of data points shown in each subfigure. The values of MSD are reported in Table 2. Using Eq. (18) for extrapolation needs discretion if  $Stk/Fr$  is out of the provided dynamic range.

In summary, taking the inter-species variabilities in pulmonary anatomy and the differences in RH and temperature, Eq. (18) can be used as a more accurate scale-up method to estimate the deposition of water droplets for both rat and human, compared with using the body weight and airway surface area ratios as the scale-up factors. Specifically, the ratio of the human bodyweight over the rat

**Table 2**  
Coefficients in Eq. (18).

	$C_1$	$C_2$	$C_3$	$C_4$	$C_5$	MSD
Deposition in the Extrathoracic Region and Trachea ( $DF_{ET}$ )	$8.86 \times 10^{-1}$	25.71	1.25	$-8.84 \times 10^{-1}$	$-2.43 \times 10^3$	$2.55 \times 10^{-4}$
Total Deposition Fraction in the Whole Respiratory Systems	$-9.67 \times 10^{-1}$	$-1.41 \times 10^4$	1.52	$9.83 \times 10^{-1}$	7.58	$6.90 \times 10^{-4}$

bodyweight is 246.7. Projecting human deposition from rat deposition data using the bodyweight ratio or surface area ratio will generate unrealistic deposition fractions, which will not be accurate. Furthermore, the ratio of the surface area of the human respiratory system over that of the rat has a value of 49.3, which is not an accurate parameter for inter-species data extrapolation.

### 3.5. Effects of RH and temperature boundary conditions

The size alteration of droplets in human airways has been studied under realistic BCs (Ferron et al., 1989, 2013). However, numerical studies that consider idealized BCs (Asgharian, 2004; Broday & Georgopoulos, 2001; Tian et al., 2013) with assumptions of constant temperature and RH for the entire human and rat airways indicate the possibility that the idealized BCs can significantly influence the droplet transport and deposition prediction. Therefore, to determine whether using idealized BCs is an eligible simplification from realistic BCs, simulations using idealized BCs were performed. The idealized BCs employed in this study are listed in Table 1. The droplet size change and deposition patterns in human respiratory systems using idealized BCs and realistic BCs are compared.

Figure 11 shows the RH distributions with idealized BCs along the same cross-sectional lines in Fig. 6. Specifically, since  $RH = 0.995$  at all airway walls, which is higher than the realistic RH BCs, the RH distributions in Fig. 11 are higher than those in Fig. 6. It can also be observed that using idealized BC, the inhaled airflow becomes saturated at G16, which is earlier than G17 in Fig. 6 with the realistic BCs. Accordingly, the deposition pattern and final diameters of droplets with the idealized BCs (see Fig. 12) are larger than the droplets with the same  $d_{p,i}$  shown in Fig. 8, which were predicted with the realistic BCs. Specifically, with the higher RHs at the airway walls and in the computational domain, condensation occurs when using idealized BCs, which results in the size growth of droplets with different initial diameters (see Fig. 12). Compared with the deposition pattern of droplets ( $d_{p,i} = 1 \mu\text{m}$ ) with realistic BC (see Fig. 8 (a)), droplets deposition with the idealized BCs (see Fig. 12 (a)) covers a larger area in the nasal vestibule due to longer residence time of the droplets with the condensation effect and slower evaporation effect. Figure 12 (b) demonstrates more scattered deposition patterns of droplets ( $d_{p,i} = 7 \mu\text{m}$ ) under the idealized BCs than realistic BCs (see Fig. 8 (d)). However, although the size change dynamics are different, the deposition patterns in the extrathoracic region and the trachea are similar. Figure 12 (c) shows that droplets with  $d_{p,i} = 15 \mu\text{m}$  deposited in the nasal cavity, pharynx, and oral cavity are similar to the deposition patterns predicted under realistic BCs (see Fig. 8 (h)). As the droplets travel deeper into the lung, the idealized BCs will lead to larger averaged droplet sizes due to the higher RH at the airway wall and the computational domain, making the inertial impaction gravitational sedimentation more dominant on droplet deposition. Therefore, a more concentrated deposition pattern can be observed in Fig. 12 (c), compared with the more scattered deposition pattern in Fig. 8 (h). Thus, droplets do not evaporate under idealized BCs as fast as those under realistic BCs, which induced noticeable deviations in predicting droplet size change dynamics and the depositions of droplets with different initial diameters.

Moreover, the GR comparisons of deposited droplets between using the idealized BCs and realistic BCs are shown in Fig. 13 (a)-(c). It is evident that idealized BCs will overpredict the droplet size compared with the realistic BC. The deviations in GR predictions increases with the increase in droplet initial diameter  $d_{p,i}$ . Specifically, GR's prediction for  $d_{p,i} = 1 \mu\text{m}$  (see Fig. 13 (a)) is less sensitive to the differences between idealized and realistic BCs. In contrast, GR prediction differences are noticeable for droplets with  $d_{p,i} = 7 \mu\text{m}$  and  $15 \mu\text{m}$  (see Figs. 13 (b) and (c)).

In addition, the influence of BCs on DF and EF predictions are also visualized (see Figs. 14 (a)-(d)). Figure 14 (a) indicates that the influence of BCs (realistic vs. idealized) on the DF of pure water droplets in the extrathoracic region and trachea is not significant. Similarly, the BC influence on DF in the TB for large droplets ( $d_{p,i} \geq 11 \mu\text{m}$ ) is negligible too (see Fig. 14 (b)). However, the idealized BC overpredicts the DF in the TB tree for droplets with an initial diameter  $1 \mu\text{m} < d_{p,i} < 11 \mu\text{m}$  (see Fig. 14 (b)). Furthermore, it can be found in Figs. 14 (c) and (d) that the idealized BC will underpredict the evaporation rate (also see Figs. 13 (a)-(c)) and EF accordingly, which lead to the overprediction total DF.

In summary, compared with using realistic BCs (see Table 1), idealized BCs can lead to noticeable overprediction in droplet size and DFs, underprediction of EFs, and differences in deposition patterns, especially for small pure water droplets. Using idealized BC may

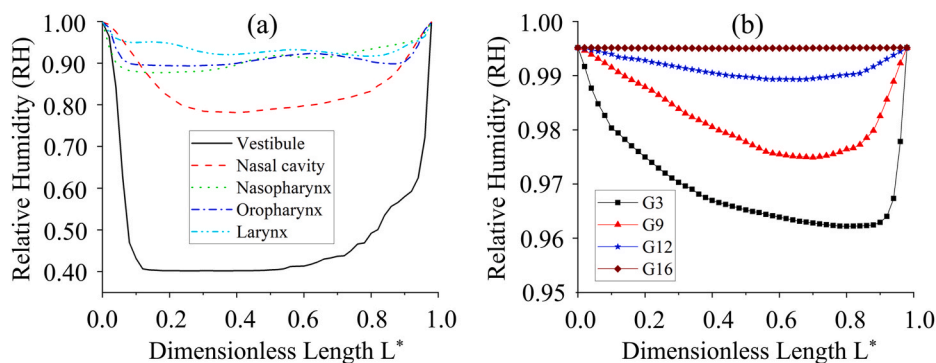


Fig. 11. Relative humidity (RH) distributions in the human respiratory system under idealized BCs: (a) selected locations in the upper airway, and (b) selected locations in the tracheobronchial (TB) tree.

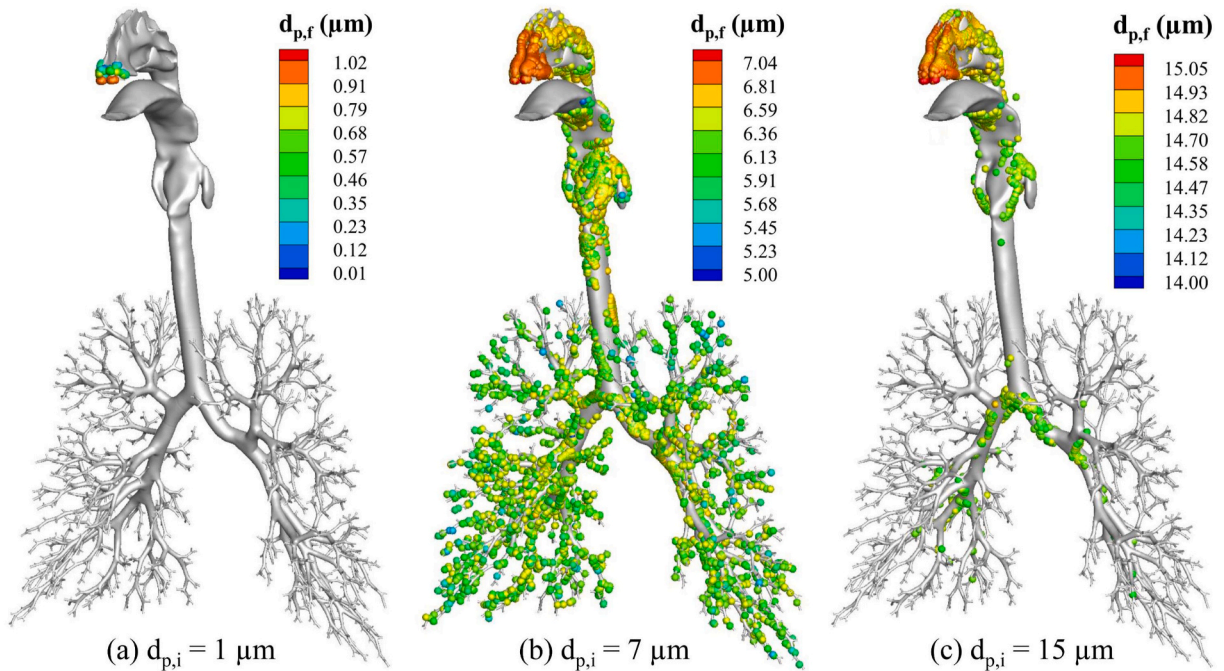


Fig. 12. Droplet deposition patterns with different initial diameters in human respiratory system under idealized BCs: (a)  $d_{p,i} = 1 \mu\text{m}$ , (b)  $d_{p,i} = 7 \mu\text{m}$  and (c)  $d_{p,i} = 15 \mu\text{m}$ .

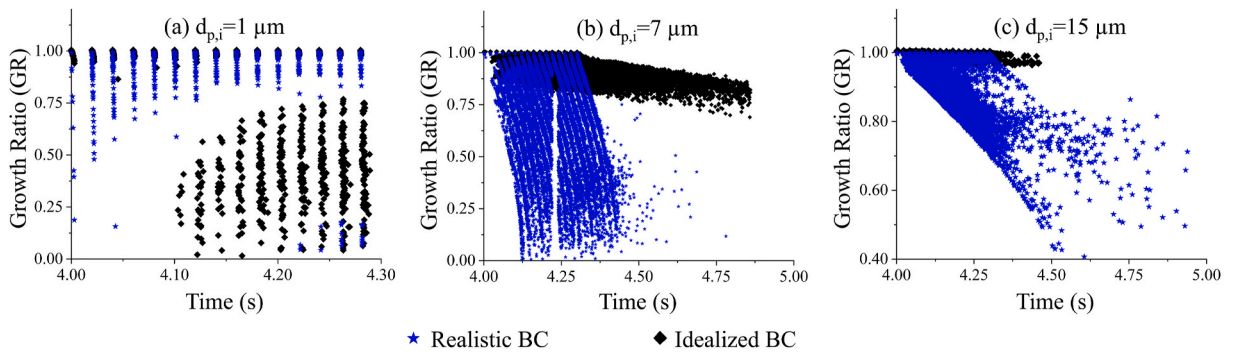


Fig. 13. Growth ratio (GR) comparisons of droplets with different initial diameters and different airways boundary conditions: (a)  $d_{p,i} = 15 \mu\text{m}$ , (b)  $d_{p,i} = 7 \mu\text{m}$ , and (c)  $d_{p,i} = 1 \mu\text{m}$ .

provide predictions that deviated from the physiologically realistic results. Realistic RH and temperature at the airway walls must be employed to accurately predict the transport, deposition, and size change dynamics of inhaled droplets.

#### 4. Conclusions

To find an accurate scale-up method from droplet deposition data in rat to human respiratory systems, the transport and deposition of pure-water droplets in both rat and human airway models were simulated. Employing realistic distribution of RH and temperature on airways walls, the transport, size change, and deposition of droplets with different initial diameters but same range of  $Stk/Fr$  were simulated in human and rat respiratory systems under resting breathing conditions. Correlations are generated for deposition fractions (DFs) as functions of  $Stk/Fr$ , which fit both human and rat data well. They can serve as the scale-up method to project human deposition based on rat studies. Key conclusions are summarized as follows, which will be further examined by *in vitro* studies in the future:

- For transient resting breathing conditions, the airflow becomes quasi-fully developed and axisymmetric in the human airways deeper than G17, and the rat airways deeper than G21. Therefore, truncated airway models or 1D network models can be employed

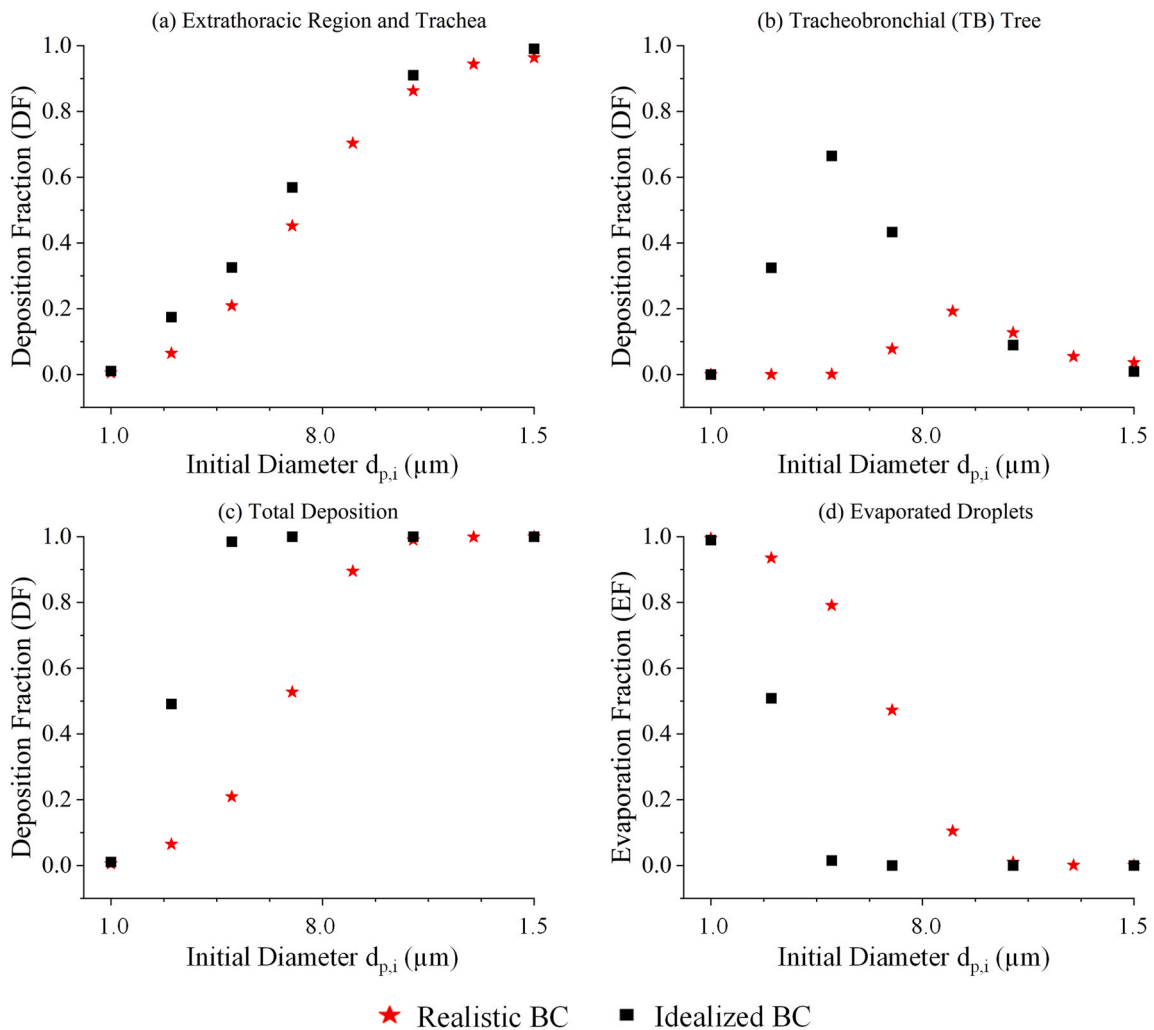


**Fig. 14.** Comparisons of predicted deposition fractions (DFs) and evaporation fractions (EFs) using realistic and idealized boundary conditions (BCs).

for the regions mentioned above when building whole-lung models with an optimized balance between computational accuracy and efficiency. However, 3D physiologically realistic airway configurations must be used from mouth/nose to G16 in the human lung and G20 in the rat lung.

- Droplets with small initial diameters shrink faster than larger ones in both human and rat airways. Larger droplets evaporated entirely at a lower rate than small droplets, causing them to reach lower airways. Droplets with the same value of  $Stk/Fr$  follow a similar DF and EF trend in both respiratory systems.
- It is not accurate to use ratios of body weights or lung surface areas between humans and rats as the scale-up factors to achieve inter-species extrapolation of droplet deposition estimations. Plotting deposition fractions (DFs) vs.  $Stk/Fr$  can unify deposition data in both human and rat airways along the same curves. The correlations are generated accordingly as the scale-up method considers the effects of inter-species differences in pulmonary anatomy and RH/temperature distributions on droplet depositions.
- Using idealized RH and temperature boundary conditions can lead to noticeable overprediction in droplet size and DFs, underprediction of EFs, and differences in deposition patterns, especially for small pure water droplets. It is necessary to employ realistic RH and temperature at the airway walls to accurately predict the transport, deposition, and size change dynamics of inhaled droplets in both human and rat respiratory systems.

## 5. Limitations of the study and future work

In this study, the following assumptions are made:

- (1) Numerical simulations were performed for resting breathing conditions only. Therefore, the research findings might not be applicable to other breathing conditions.
- (2) Pure water droplets were employed in this study, which allows droplets to evaporate completely. However, real-world infectious virus-laden droplets and toxic droplets are multi-component and will not change entirely to vapor/gas phases (Haghnegahdar et al., 2019).
- (3) Equation (18) and the coefficients may vary with other human and rat respiratory system configurations due to the inter-subject variabilities.

To address the limitations mentioned above which are associated with the assumptions and simplifications made in the present study, future work includes:

- (1) Breathing patterns with different intensities will be considered for both human and rat models for studying droplet behavior, which will give more comprehensive deposition and size change data for a generalized scale-up method between human and rat, which will not be limited to resting condition only.
- (2) Multi-component virus-laden droplets will be simulated, which will provide the capability of tracking the transport of viruses and nuclei after the possible total evaporation of water. It is worth mentioning that the virus-laden nuclei diameters range from 80 nm to 120 nm for the influenza A virus (IAV).
- (3) More airway configurations of human and rat will be employed for the CFPD simulations to consider the inter-subject variabilities.

### Declaration of competing interest

The authors declare that they have no known competing financial interests or personal relationships that could have appeared to influence the work reported in this paper.

### Acknowledgments

This work was supported by funds from the Oklahoma Center for Adult Stem Cell Research, NIH Center of Biomedical Research Excellence (COBRE) (P20 GM103648), Oklahoma State University Research Activity funding. The authors also thank the COBRE Animal Models Core for assistance and Huan Song for expert technical assistance. The use of Ansys software (Canonsburg, PA, USA) as part of the Ansys-CBBL academic partnership agreement is gratefully acknowledged (Dr. Thierry Marchal, Global Industry Director). The authors are grateful for the supply of the rat respiratory system model by Drs. R. Corley and A. Kuprat (Pacific Northwest National Laboratory). The authors would like to thank Mrs. Pam Reynolds for constructive feedback and English language editing.

### References

- Asgharian, B. (2004). A model of deposition of hygroscopic particles in the human lung. *Aerosol Science and Technology*, 38(9), 938–947. <https://doi.org/10.1080/027868290511236>
- Bird, R. B., Stewart, W. E., & Lightfoot, E. N. (1960). *Transport phenomena*.
- Brechtel, F. J., & Kreidenweis, S. M. (1999). Predicting particle critical supersaturation from hygroscopic growth measurements in the humidified tdma. Part I: Theory and sensitivity studies. *Journal of the Atmospheric Sciences*, 57, 1854–1871. [https://doi.org/10.1175/1520-0469\(2000\)057<1854:PPCSFH>2.0.CO;2](https://doi.org/10.1175/1520-0469(2000)057<1854:PPCSFH>2.0.CO;2)
- Brodady, D. M., & Georgopoulos, G. (2001). Growth and deposition of hygroscopic particulate matter in the human lungs *Aerosol Science and Technology*, 34(1), 144–159. <https://doi.org/10.1080/02786820118725>
- Calmet, H., Kleinstreuer, C., Houzeaux, G., Kolanjiyil, A. V., Lehmkuhl, O., Olivares, E., et al. (2018). Subject-variability effects on micron particle deposition in human nasal cavities. *Journal of Aerosol Science*, 115, 12–28.
- Chen, X., Feng, Y., Zhong, W., & Kleinstreuer, C. (2017). Numerical investigation of the interaction, transport and deposition of multicomponent droplets in a simple mouth-throat model. *Journal of Aerosol Science*, 105, 108–127. <https://doi.org/10.1016/j.jaerosci.2016.12.001>
- Cheng, K. H., Cheng, Y. S., Yeh, H. C., Guilmette, R. A., Simpson, S. Q., Yang, Y. H., et al. (1996). In vivo measurements of nasal airway dimensions and ultrafine aerosol deposition in the human nasal and oral airways. *Journal of Aerosol Science*, 27(5), 785–801. [https://doi.org/10.1016/0021-8502\(96\)00029-8](https://doi.org/10.1016/0021-8502(96)00029-8)
- Clarkson, M. R., Magee, C., & Brenner, B. M. (2011). *Pocket companion to brenner and rector's the kidney* (2nd ed.).
- Corley, R. A., Kabilan, S., Kuprat, A. P., Carson, J. P., Jacob, R. E., Minard, K. R., ... Einstein, D. R. (2015). Comparative risks of aldehyde constituents in cigarette smoke using transient computational fluid dynamics/physiologically based pharmacokinetic models of the rat and human respiratory tracts. *Toxicological Sciences*, 146(1), 65–88. <https://doi.org/argo.library.okstate.edu/10.1093/toxsci/kfv071>
- Corley, R. A., Kabilan, S., Kuprat, A. P., Carson, J. P., Minard, K. R., Jacob, R. E., ... Enistein, D. R. (2012). Comparative computational modeling of airflows and vapor dosimetry in the respiratory tract of rat, monkey, and human. *Toxicological Sciences*, 128(2), 500–516. <https://doi.org/10.1093/toxsci/kfs168>
- Dai, Y. T., Chang, C. P., Tu, L. J., & Hsu, D. J. (2007). Development of a taiwanese head model for studying occupational particle exposure. *Inhalation Toxicology*, 19, 383–392. <https://doi.org/10.1080/08958370601174792>
- Ferron, G. A., Oberdorster, G., & Henneberg, R. (1989). Estimation of the deposition of aerosolized drugs in the human respiratory tract due to hygroscopic growth. *Journal of Aerosol Medicine*, 2(3), 271–284. <https://doi.org/10.1089/jam.1989.2.271>
- Ferron, G. A., Upadhyay, S., Zimmermann, R., & Karg, E. (2013). Model of the deposition of aerosol particles in the respiratory tract of the rat. II. Hygroscopic particle deposition. *Journal of Aerosol Medicine and Pulmonary Drug Delivery*, 26(2), 101–118. <https://doi.org/10.1089/jamp.2011.0965>
- Gerde, P., Cheng, Y. S., & Medinsky, M. A. (1991). In Vivo deposition of ultrafine aerosols in the nasal airway of the rat. *Toxicological Sciences*, 16(2), 330–336. <https://doi.org/10.1093/toxsci/16.2.330>
- Golli, S. E., Arnaud, G., Bricard, J., & Treiner, C. (1977). Evaporation of volatile solvent from saline multi-component droplets carried in a stream of air. *Journal of Aerosol Science*, 8(1), 39–54. [https://doi.org/10.1016/0021-8502\(77\)90061-1](https://doi.org/10.1016/0021-8502(77)90061-1)
- Golshahi, L., Noga, M. L., Thompson, R. B., & Finlay, W. H. (2011). In vitro deposition measurement of inhaled micrometer-sized particles in extrathoracic airways of children and adolescents during nosebreathing. *Journal of Aerosol Science*, 42, 474–488. <https://doi.org/10.1016/j.jaerosci.2011.04.002>

- Haghnegahdar, A., Feng, Y., Chen, X., & Lin, J. (2018). Computational analysis of deposition and translocation of inhaled nicotine and acrolein in the human body with e-cigarette puffing topographies. *Aerosol Science and Technology*, 52(5), 483–493.
- Haghnegahdar, A., Zhao, J., & Feng, Y. (2019). Lung aerosol dynamics of airborne influenza A virus-laden droplets and the resultant immune system responses: An in silico study. *Journal of Aerosol Science*, 134, 34–55. <https://doi.org/10.1016/j.jaerosci.2019.04.009>
- Hayati, H., & Feng, Y. (2020). A precise scale-up method to predict particle delivered dose in a human respiratory system using rat deposition data: An in silico study. In *2020 design of medical devices conference* (pp. 1–6). <https://doi.org/10.1115/DMD2020-9060>
- Hayati, H., Goharrizi, A. S., Salmanzadeh, M., & Ahmadi, G. (2019). Numerical modeling of particle motion and deposition in turbulent wavy channel flows. *Scientia Iranica*, 26(4), 2229–2240. <https://doi.org/10.24200/sci.2019.21405>
- Kelly, J. T., Asgharian, B., Kimbell, J. S., & Wong, B. A. (2004). Particle deposition in human nasal airway replicas manufactured by different methods. Part I: Inertial regime particles. *Aerosol Science and Technology*, 38(11), 1063–1071. <https://doi.org/10.1080/027868290883360>
- Kelly, J. T., Bobbitt, C. M., & Asgharian, B. (2001). In vivo measurement of fine and coarse aerosol deposition in the nasal airways of female Long-Evans rats. *Toxicological Sciences*, 64(2), 253–258. <https://doi.org/argo.library.okstate.edu/10.1093/toxsci/64.2.253>
- Kitaoka, Hiroko (2011). A 4D model generator of the human lung. *Forma*, 26, 19–24.
- Kolanjiyil, A. V., & Kleinstreuer, C. (2017). Computational analysis of aerosol-dynamics in a human whole-lung airway model. *Journal of Aerosol Science*, 114, 301–316. <https://doi.org/10.1016/j.jaerosci.2017.10.001>
- Kolanjiyil, A. V., Kleinstreuer, C., Kleinstreuer, N. C., Pham, W., & Sadikot, R. T. (2019). Mice-to-men comparison of inhaled drug-aerosol deposition and clearance. *Respiratory Physiology & Neurobiology*, 260, 82–94. <https://doi.org/10.1016/j.resp.2018.11.003>
- Kreidenwey, S. M., Koehler, K., DeMott, P. J., Prenni, A. J., Carrico, C., & Ervens, B. (2005). Water activity and activation diameters from hygroscopicity data – Part I: Theory and application to inorganic salts. *Atmospheric Chemistry and Physics*, 5, 1357–1370. <https://doi.org/10.5194/acp-5-1357-2005>
- Longest, P. W., & Hindle, M. (2012). Condensational growth of combination drug-excipient submicrometer particles for targeted high efficiency pulmonary delivery: Comparison of CFD predictions with experimental results. *Pharmaceutical Research*, 29(3), 707–721. <https://doi.org/10.1007/s11095-011-0596-1>
- Longest, P. W., & Kleinstreuer, C. (2005). Computational models for simulating multicomponent aerosol evaporation in the upper respiratory airways. *Aerosol Science and Technology*, 39(2), 124–138. <https://doi.org/10.1080/027868290908786>
- Longest, P. W., Tian, G., & Hindle, M. (2011). Improving the lung delivery of nasally administered aerosols during noninvasive ventilation—an application of enhanced condensational growth (ECG). *Journal of Aerosol Medicine and Pulmonary Drug Delivery*, 24(2), 103–118. <https://doi.org/10.1089/jamp.2010.0849>
- Longest, P. W., & Xi, J. (2008). Condensational growth may contribute to the enhanced deposition of cigarette smoke particles in the upper respiratory tract. *Aerosol Science and Technology*, 42, 579–602. <https://doi.org/10.1080/02786820802232964>
- Luo, H. Y., & Liu, Y. (2009). Particle deposition in a CT-scanned human lung airway. *Journal of Biomechanics*, 42, 1869–1876. <https://doi.org/10.1016/j.jbiomech.2009.05.004>
- Menter, F. R., Langtry, R. B., Likki, S. R., Suzen, Y. B., Huang, P. G., & Völker, S. (2006). A correlation-based transition model using local variables— part I: Model formulation. *Journal of Turbomachinery*, 128, 413–422. <https://doi.org/10.1115/1.2184352>
- Nielsen, G. D., & Koponen, I. K. (2018). Insulation fiber deposition in the airways of men and rats. A review of experimental and computational studies. *Regulatory Toxicology and Pharmacology*, 94, 252–270. <https://doi.org/10.1016/j.yrtph.2018.01.021>
- Nikander, K., Prince, I., Coughlin, S., Warren, S., & Taylor, G. (2010). Mode of breathing-tidal or slow and deep-through the I-neb Adaptive Aerosol Delivery (AAD) system affects lung deposition of (99m)Tc-DTPA. *Journal of Aerosol Medicine and Pulmonary Drug Delivery*, 23, 37–43. <https://doi.org/10.1089/jamp.2009.0786>
- Saffman, P. G. (1965). The lift on a small sphere in a slow shear flow. *Journal of Fluid Mechanics*, 22(2), 385–400. <https://doi.org/10.1017/S00222112065000824>
- Schroeter, J. D., Kimbell, J. S., Asgharian, B., Tewksbury, E. W., & Singal, M. (2012). Computational fluid dynamics simulations of submicrometer and micrometer particle deposition in the nasal passages of a Sprague-Dawley rat. *Journal of Aerosol Science*, 43, 31–44. <https://doi.org/10.1016/j.jaerosci.2011.08.008>
- Shang, Y., Dong, J., Inthavong, K., & Tu, J. (2015). Comparative numerical modeling of inhaled micron-sized particle deposition in human and rat nasal cavities. *Inhalation Toxicology*, 27(13), 694–705. <https://doi.org/10.3109/08958378.2015.1088600>
- Stahlhofen, W., Rudolf, G., & James, A. C. (1989). Intercomparison of experimental regional aerosol deposition data. *Journal of Aerosol Medicine*, 2(3), 285–308. <https://doi.org/10.1089/jam.1989.2.285>
- Tian, G., Longest, P. W., Li, X., & Hindle, M. (2013). Targeting aerosol deposition to and within the lung airways using excipient enhanced growth. *Journal of Aerosol Medicine and Pulmonary Drug Delivery*, 26(5), 248–265. <https://doi.org/10.1089/jamp.2012.0997>
- Whitaker, S. (1972). Forced convection heat transfer correlations for flow in pipes, past flat plates, single cylinders, single spheres, and for flow in packed beds and tube bundles. *AIChE Journal*, 18(2), 361–371. <https://doi.org/10.1002/aic.690180219>
- Xi, J., Kim, J., Si, X. A., Corley, R. A., & Zhou, Y. (2016). Modeling of inertial deposition in scaled models of rat and human nasal airways: Towards in vitro regional dosimetry in small animals. *Journal of Aerosol Science*, 99, 78–93. <https://doi.org/10.1016/j.jaerosci.2016.01.013>
- Zhang, Z., Kleinstreuer, C., & Feng, Y. (2012). Vapor deposition during cigarette smoke inhalation in a subject-specific human airway model. *Journal of Aerosol Science*, 53, 40–60. <https://doi.org/10.1016/j.jaerosci.2012.05.008>